PHASE TRANSITION MECHANISMS FOR ELECTROCHEMICAL SYSTEMS WITH INTERFACIAL ION TRANSFER

by

CAITLYN CANNAN

A THESIS

Presented to the Department of Chemistry and Biochemistry
and the Robert D. Clark Honors College
in partial fulfillment of the requirements for the degree of
Bachelor of Science

May 2025

An Abstract of the Thesis of

Caitlyn Cannan for the degree of Bachelor of Science
in the Department of Chemistry and Biochemistry to be taken June 2025

Title: Phase Transition Mechanisms for Electrochemical Systems with Interfacial Ion Transfer

Approved: *Paul Kempler, Assistant Professor*
Primary Thesis Advisor

Electrochemistry plays a crucial role in the development of durable and sustainable devices aimed at fostering an environmentally friendly infrastructure. To advance these technologies, it is essential to understand the underlying degradation mechanisms. Interfacial ion transfer is often a limiting factor in electrochemical devices, as it can serve as a rate-limiting step in charge transfer within electrochemical cells. This thesis explores the mechanisms of interfacial ion transfer in model systems, with a focus on how temperature affects the kinetics of corrosion at solid-solid interfaces and the behavior of cation insertion during phase transitions in Prussian Blue thin films.

In Chapter 1, the research investigates copper deposition and corrosion to gain insights into degradation mechanisms relevant to solar technology. The study examines the contributions of various kinetic mechanisms in temperature-dependent systems for copper (Cu) monolayer formation. Qualitative results indicate that at lower temperatures, nucleation limits the rate of Cu monolayer formation, while at elevated temperatures, Cu overcomes the nucleation barrier, leading to less ordered deposition or stripping. This framework for ion transfer enhances our understanding of corrosion processes and provides a foundation for examining the mechanistic effects across a range of temperatures.

Chapter 2 examines the impact of interfacial ion transfer on the degradation of electrode materials used in energy storage devices. Specifically, a Prussian Blue thin film is employed as a model system to explore the insertion mechanism of various cations across a range of concentrations. The hypothesis is that this mechanism will exhibit kinetics similar to those of adsorption reactions. The research highlights the complications that arise from the dynamic interactions between cations and the PB lattice, requiring modifications to standard models in order to accurately fit the data. By uncovering the underlying phase transition mechanisms, this work contributes to advancing the understanding of interfacial ion transfer in insertion/removal electrochemical systems.

The conclusions drawn from this thesis not only inform the design of sustainable energy storage devices but also improve our ability to address material degradation and optimize performance in electrochemical applications.

Acknowledgements

I would first like to sincerely thank Professors Paul Kempler and Marisa King for serving on my thesis committee and for their continued support throughout the writing process. I am also grateful to Ms. Miriam Jordan of the Clark Honors College for providing the thesis template and ensuring that this document meets all formatting requirements. I especially want to express my deep appreciation to Professor Kempler for his invaluable teaching, mentorship, and guidance throughout my time writing this thesis and during my years in the lab. I would also like to acknowledge Professor Shannon Boettcher for inspiring my interest in electrochemistry and for introducing me to the world of applied research. My Ph.D. mentor, Kira Thurman, provided mentorship that was instrumental in teaching me the skills and knowledge that have shaped my experience as a researcher. I am also grateful to all members of the Boettcher and Kempler research groups for their kindness, insightful discussions, and support. In particular, I would like to thank Nadia Barnard for her friendship and encouragement through many late nights and early mornings in lab. I could not have completed this thesis without the unwavering support of my friends and family, with special thanks to my parents for their constant encouragement. Finally, I gratefully acknowledge the funding that made this research possible: the Robert Ragel Scholarship, the Presidential Undergraduate Research Scholarship, the Liquid Sunlight Alliance, funded by the U.S. Department of Energy, Office of Science, Office of Basic Energy Sciences, and the National Science Foundation for funding the CCI Phase I: Center for Interfacial Ionics at University of Oregon.

Table of Contents

List of Figures

List of Tables

Introduction

Research in Electrochemistry

Electrochemistry is an important subdiscipline of chemistry which is creating state-of-the-art technologies for clean energy and the reduction of carbon emissions. The field aims to create both small scale and industrial changes to protect the environment while being cost efficient. As the past few decades have created extreme energy and climate problems, we are facing the need for clean and efficient solutions. With projections claiming the world's energy consumption will increase from 30% to 50% in the next 20 years, we need solutions fast.[1] As many countries commit to cleaner societal infrastructure, there is growing optimism that a more sustainable future can be achieved, with electrochemistry serving as a key tool for this progress.[2]

Electrochemistry is defined as the study of chemical reactions that occur due to the movement of electrons and ions within a system. These reactions can be categorized into two main types: (1) the use of electricity to drive a chemical reaction, or (2) chemical reactions that produce electricity. Current research in electrochemistry focuses on several major themes, as illustrated in Figure 1: advancing the fundamental understanding necessary to optimize the durability of electrochemical systems and devices, optimizing water-splitting technologies for clean hydrogen (H_2) production, and scaling up energy storage solutions.

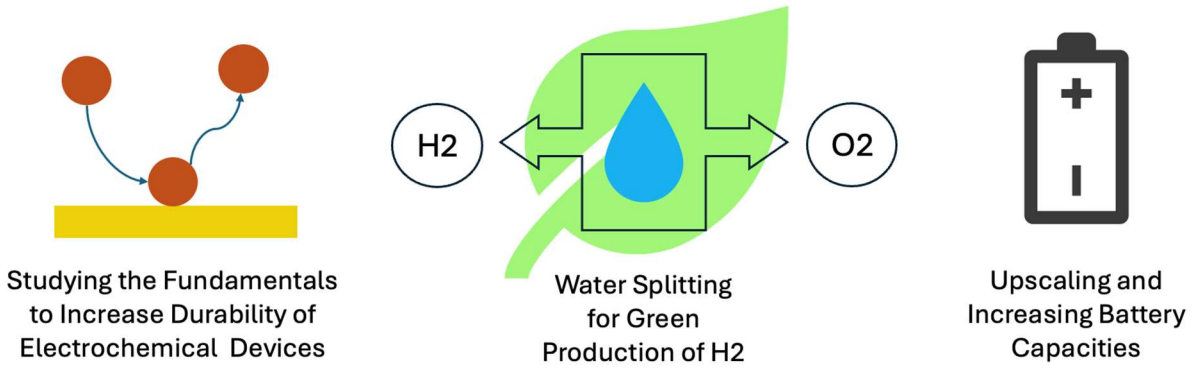

Figure 1: Three Major Areas of Electrochemistry Research

The three major areas of interest in electrochemistry research, both nationally and within the Kempler Lab.

Importance of Ion Transfer

This thesis project is centered around understanding the interfacial ion transfer mechanism for electrochemical systems with phase transitions. While electron transfer processes have been extensively studied and are supported by well-established models, the same level of understanding does not yet exist for ion transfer.[3] Ion transfer across electrode–electrolyte interfaces significantly affects, and often limits, the performance of a wide range of electrochemical devices.[4] The lack of knowledge has serious implications, contributing to issues such as corrosion and failures in energy storage systems. A deeper mechanistic understanding of ion transfer is essential to drive improvements in the design and durability of electrochemical technologies.

Electrochemistry allows one to construct model systems for fundamental investigations into ion transfer mechanisms. A model system uses well-known electrochemical cells in which one can change key variables and analyze the resulting changes to what has previously been understood. By examining the interactions at the electrode–electrolyte interface, the critical ion transfer step can be isolated and analyzed from multiple perspectives.

Kinetic analysis of interfacial ion transfer is vital to the development of electrochemical devices. Through the use of the model systems, ion transfer can be studied from a fundamental standpoint, allowing data to inform how ions interact with different environments. Additionally, kinetic studies can fuel an understanding if ion-transfer is the rate-limiting step in an electrochemical cell and provide insights into mitigating these issues.[5] Using simple molecules, for which one knows a majority of the physical and chemical properties, one can better understand the underlying ion transfer mechanism without needing to account for additional complexities. By employing simple molecules, whose physical and chemical properties are well characterized, the underlying mechanisms of ion transfer can be elucidated without needing to account for additional complexities. Once these fundamental principles are better understood, they can be extended to more complex electrochemical systems, ultimately contributing to the design of improved devices for clean energy infrastructure.

Copper as a Model System

Copper metal is extensively utilized in electrochemical energy devices such as wiring, circuitry, and wind turbines.[6] However, a significant limitation is that copper, like most metals, undergoes corrosion, which reduces both its lifespan and effectiveness. Corrosion doesn't only affect the quality of devices; environmentally, it has been found the amount of material lost due to corrosion is proportional to the amount of carbon dioxide produced.[7] Investigating corrosion mechanisms at the electrode–electrolyte interface can provide critical insights into strategies for mitigating these negative effects. Copper can be deposited in single layers using underpotential deposition (UPD) allowing us to observe kinetic mechanisms right at the interface.[8] A fundamental understanding of these corrosion reactions will inform industrial practices and guide

future experimental efforts, ultimately improving the durability of copper-based electrochemical devices.

Prussian Blue as a Model System

Studying phase transitions to illuminate the durability of electrochemical systems can be expanded to energy storage materials. In many energy storage devices, electrodes commonly undergo phase transitions between their charged and discharged states.[9] To study energy storage materials, we can investigate the ion transfer kinetic mechanisms during the phase transition of Prussian Blue (PB) to Prussian White (PW). PB films have recently been investigated as a cathode material in batteries.[10] A model system can be established using electrodeposited thin films of PB to study ion insertion and removal without the complications of diffusion. Investigating ion cycling and the associated transfer mechanisms can provide critical information about electrode degradation as charged ions are repeatedly inserted and extracted over time. Given the growing demand for clean energy solutions, understanding the kinetic mechanisms underlying energy storage is vital for advancing the scalability and performance of battery technologies.

Chapter 1: Copper Underpotential Deposition (UPD) and it's Corrosion Mechanisms

1.1 Background and Literature

Technology and industrial processes from the past few centuries have created extreme energy and climate problems. With the knowledge that irreversible damage to the earth and atmosphere has already occurred, projections claim the world's energy consumption will continue to increase from 30% to 50% in the next 20 years.[1] Society is facing the need for clean, efficient solutions and fast.

Figure 2: Role of Copper in Solar Technology.[6]

Copper (Cu) metal is essential for the electrochemical field as it is an exceptional catalyst for most electrochemical devices with its high conductivity. Cu is fashioned into conductive wires, electrical grids, and is used in wind turbines; the applications range from household appliances to energy conversion technologies (Figure 2).[6] However, Cu devices corrode, deteriorating from

oxidation reactions which limit quality and durability. Corrosion of Cu and other electrochemical metals is predominant enough that the amount of industrial product lost due to corrosion is proportional to the amount of CO_2 produced.[11] Decreasing emissions by slowing and/or limiting corrosion is possible when the mechanism is understood.

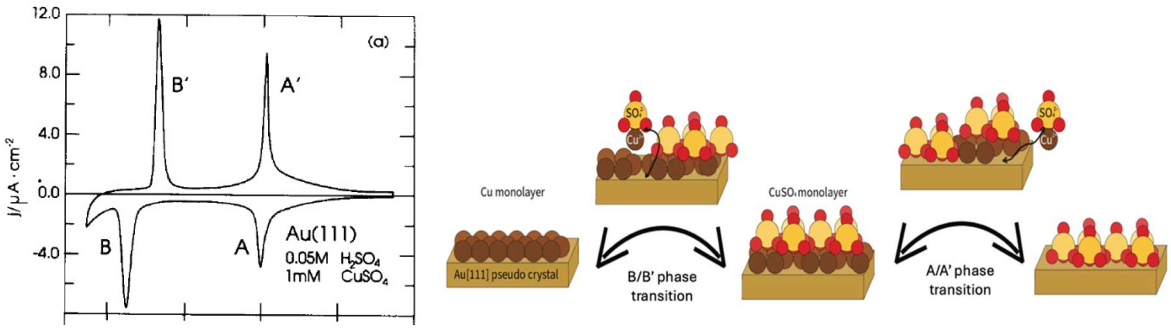

Figure 3: Copper Phase Transitions During UPD onto Au(111) Electrode

Literature graph showing copper UPD onto an Au single crystal at 5 mV/s (left) and mechanism of Cu and $CuSO_4$ monolayers depositing and stripping off as seen in graph (right).[12]

The mechanism of Cu corrosion can be based on underpotential deposition where we can examine the interactions of a solid-solid interface. Underpotential deposition (UPD) causes a single monolayer, or submonolayer, to form on the surface of a substrate metal resulting from an electrochemical potential.[8] By studying a single layer of deposited metal, we can use techniques to observe the mechanism of the copper atom onto these electrodes solid-solid interface. The verification of an adlayer of Cu from UPD can be seen with STM or other imaging techniques by the characteristic $(\sqrt{3} * \sqrt{3})$R30° structure of a single layer.[13] The cyclic voltammetry (CV) technique gives peaks which represent the phase transition during reduction and oxidation of multi-step mechanisms for the deposition and corrosion of copper. The shape of the peaks gives information on the quality of the monolayer and the mechanism in which it was deposited.[12]

Sharp peaks correlate to a well-ordered monolayer surface while broader peaks imply a disordered surface. Figure 3 displays a CV showing the phase transitions for Cu UPD onto an Au(111) electrode along with a pictorial description of the process.

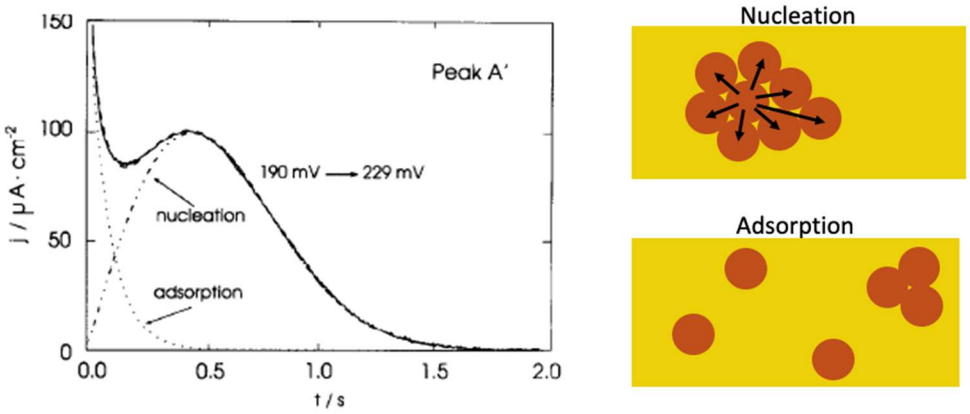

Figure 4: Current Transient Mechanisms

Literature current transient broken down into adsorption and nucleation characteristics for the A' peak (left). Pictorial representation of the adsorption and nucleation mechanisms (right).[12]

The UPD of Cu has been found to occur as a combination of two kinetic mechanisms: adsorption and nucleation. Figure 4 differentiates between the adsorption and nucleation mechanisms both graphically and pictorially. Adsorption can be analogized as paint splatter, atoms deposit or strip off an electrode randomly. On the other hand, nucleation is thermodynamically controlled; Cu atoms will systematically attach or leave the surface at energetically favorable positions, usually near other Cu atoms due to their attractive nature. Chronoamperometry (CA) instantaneously changes the cell potential and records how the system returns to its equilibrium state. The shape of CA current transients, current output over time at a specific potential, is used to differentiate between the two mechanism.[14] Hölzle and Kolb mathematically describe nucleation and adsorption as separate mechanisms (Eq. 1).[12] The first

term containing k_1 and k_2 describes the Gaussian-curved nucleation characteristic and the second exponential term (with k_3 and k_4) describes the adsorption feature. By extracting the rate constants for nucleation and adsorption separately, a quantitative measure for the influence of each mechanism can be established.

$$j(t) = [k_1 * t * \exp(-k_2 * t^2)] + [k_3 * \exp(-k_4 * t)] \quad (1)$$

Nucleation and adsorption characteristics for a system are highly variable in experimental conditions. Temperature is one external factor that controls the rate of the reaction, and when studied, can help develop an understanding of energy barriers for these electrochemical reactions. Gaining insight into temperature-dependent chemical mechanisms is essential since most electrochemical systems operate at elevated temperatures. Some research has been done to understand the change in the system when heated, yet there is disagreement in the quantitative description of the rates at which the mechanism occurs. One study found the charge density associated with Cu UPD did not reveal any temperature-dependence.[15] Alternatively, another study found temperature can significantly change the structure of deposited adlayers of Cu, a higher temperature allowing for higher diffusion rates.[16]

1.2 The Research Question

In this chapter, experiments attempt to describe how the kinetic mechanism of corrosion at a solid-solid interface is impacted by temperature for a Cu monolayer. The hypothesis is that at colder temperatures, the rate of Cu monolayer formation will be more limited by the kinetics of nucleation. On the opposite end, at elevated temperatures, Cu will more readily overcome the nucleation barrier, and monolayers will be less ordered as they are deposited or stripped. The mechanistic analysis used in this paper can be applied to understanding other charge transfer

systems. Continuing to study the mechanism for ion transfer of electrochemical materials can provide insight into deterioration mechanisms and inform the fabrication of more sustainable devices.

1.3 Results and Discussion

To study the phase transitions of Cu UPD, cyclic voltammograms were taken at various experimental conditions. Figure 5 overlays the CV graphs for two different temperature conditions.

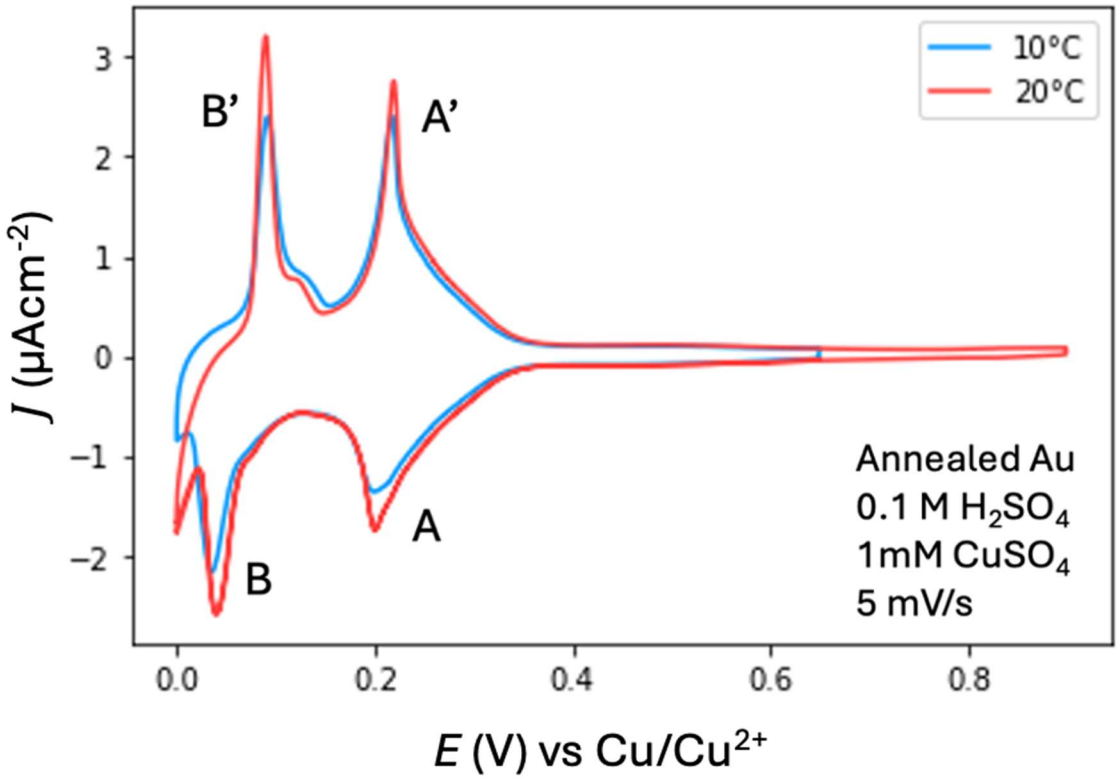

Figure 5: CV of Cu UPD at Varying Temperatures

Cyclic voltammograms (CVs) for copper deposition on an Au(111)-prepared electrode in $CuSO_4$ at 10°C and 20°C. Labeled peaks correspond to the mechanism illustrated in Figure 3.

In the CVs, as a negative charge is applied to the cell, peaks show an initial transition depositing a stable layer of $CuSO_4$ on the surface. Continuing to a more negative potential causes the sulfonate ion to leave, creating a monolayer of Cu. Running a reverse scan, in the positive direction, shows the same two-phase system. The A/A' transition has a broader peak compared to the B/B' transition. An explanation for this comes from the attraction between Cu atoms and the Au(111) surface. Referring to the deposition, $CuSO_4$ molecules are stable in electrolytes until the electrode charge requires molecules to be added to the surface. As you continue to increase the charge, and the sulfonate atoms detached, the solid copper atoms are more attracted to the charged electrode surface than the solution.

Another point of analysis is the position of the forward and reverse peaks in reference to each other. For the first phase transition, the A and A' peaks are both centered at about 0.2 V and are considered reversible. A reversible phase transition is in equilibrium; at any point in the deposition/stripping process, a little change in $CuSO_4$ coverage can occur without having to complete the transition. In contrast, the B and B' transition, with a separation of about 0.1 V, is irreversible. When a small amount of Cu is put on the surface, to take it off, a full layer of Cu would need to be deposited first.

Between the 10 °C and 20 °C systems, the broadness and reversibility of the phase transitions are consistent. A difference is seen in the current density of the peaks, the cooler temperature has lower peak heights even after normalization. Across the runs, the electrode may have had a different surface structure, however, another hypothesis is that colder temperatures slow the kinetics of ion transfer and therefore less coverage is seen. The effect of temperature is more prevalent in the CA graphs when comparing the influence of nucleation and adsorption

characteristics. Figure 6 presents the current transients for the A and A' peaks across the two experimental temperatures.

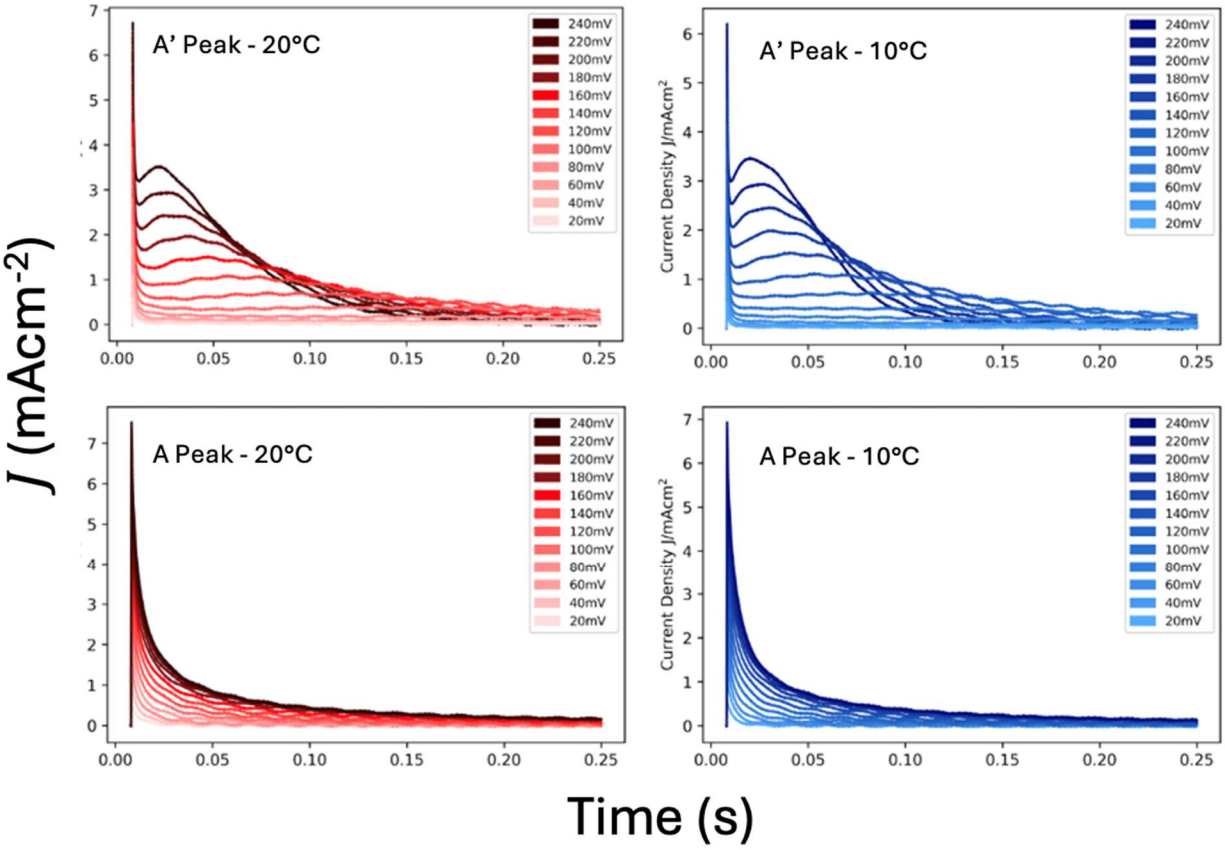

Figure 6: Current Transitions of A/A' Peaks at Varying Temperatures

Current transients for the A and A' peaks corresponding to the CVs in Figure (5), recorded at 20°C (left) and 10°C (right).

For each of the graphs above, a range of current transients show the mechanism for which the cell returns to its equilibrium condition when the potential is instantaneously changed in increments of 20 mV. From visual analysis, there are two major takeaways: one between the A and A' peaks and one between the 10 °C and 20 °C data.

It is interesting that although the A and A' peaks are reversible as seen in the CVs from Figure 5, the mechanisms between the two are vastly different. The A peak contains only

exponential decay, inferring a non-ordered adsorption of $CuSO_4$ atoms onto the Au(111) surface. An explanation for this is similar to why the A/A' peaks are broadened. The $CuSO_4$ molecules are stable in the electrolyte and will be randomly attached to the electrode to balance the changing charge in the cell. For the A' peak, there are both nucleation and adsorption characteristics. As a full monolayer of the $CuSO_4$ exists at the beginning potential, to strip the molecules, a nucleation barrier must be overcome. The nucleation barrier is due to the attractive energy between Cu atoms on the surface which are more stable coordinated together than apart in solution.

Between the temperature runs, there is no significant difference in the adsorption for peak A. In both cases, the $CuSO_4$ molecules are working to create a monolayer by randomly attaching to the surface. However, there is a slight lowering in the magnitude of the 10°C peaks, which agrees with the CV data. Comparatively, the A' peaks do show a noticeable difference. There is more nucleation characteristic for the cooler temperature run, seen as a stronger Gaussian peak. As colder temperatures slow the kinetics of the reaction, the theory is that when the potential increases, the system is more able to "choose" the most favorable molecule to strip off the surface. The molecule with the lowest energy is the one with the least surface contact points; $CuSO_4$ molecules at the edges of the monolayer will be more easily removed when the kinetics of the system do not require a fast upheaval from the surface. At higher temperatures, the amount of energy in the system occasionally requires the non-favorable $CuSO_4$ molecule, one which may be fully coordinated with other Cu atoms, to be removed before molecules at the edge of the monolayer.

1.4 Future Directions

The base of this analysis is qualitative as the quantitative analysis has not yet been completed. For the Cu UPD processes, multi-peak fitting is required to separate the exponential and Gaussian contributions. Using Hölzle and Kolb's equation (Equation 1), sets of these rate constants can be extracted. Using this analysis method with data collected at a range of temperatures, the influence of the two kinetic mechanisms can be derived as a temperature-dependent system.

1.5 Published Work

At the beginning of my time in the electrochemistry lab, I was mentored by Ph.D. student Kira Thurman, whose research focuses on advancing the fundamental understanding of copper underpotential deposition (Cu UPD) through the use of model systems. I contributed to her project by assisting with data collection, and I am a co-author on a paper published in *ACS Electrochemistry*, titled *Anions in Corrosion: Influence of Polymer Electrolytes on the Interfacial Ion Transfer Kinetics of Cu at Au(111) Surfaces*.[17] Her investigation into reversible electrochemical phase transitions and her kinetic analysis helped to motivate Chapter 2.

Chapter 2: Prussian Blue (PB) and the Mechanism for Interfacial Cation Insertion and Removal

2.1 Background and Literature

Growing energy demands have historically relied on environmentally harmful sources. However, recent advancements in clean energy technologies, particularly solar and wind, have led to remarkable improvements in efficiency and cost-effectiveness. Figure 7 illustrates the breakdown of energy generation by source from the beginning of the 20th century to the present.[18] Today, technological developments have made wind and solar energy cheaper than power generated from natural gas, coal, and oil.[19] Despite these advancements, energy storage technology remains a major bottleneck to large-scale deployment. While clean energy production is advancing rapidly, current storage capacities are insufficient to effectively store and distribute renewable energy at a scale competitive with conventional sources.

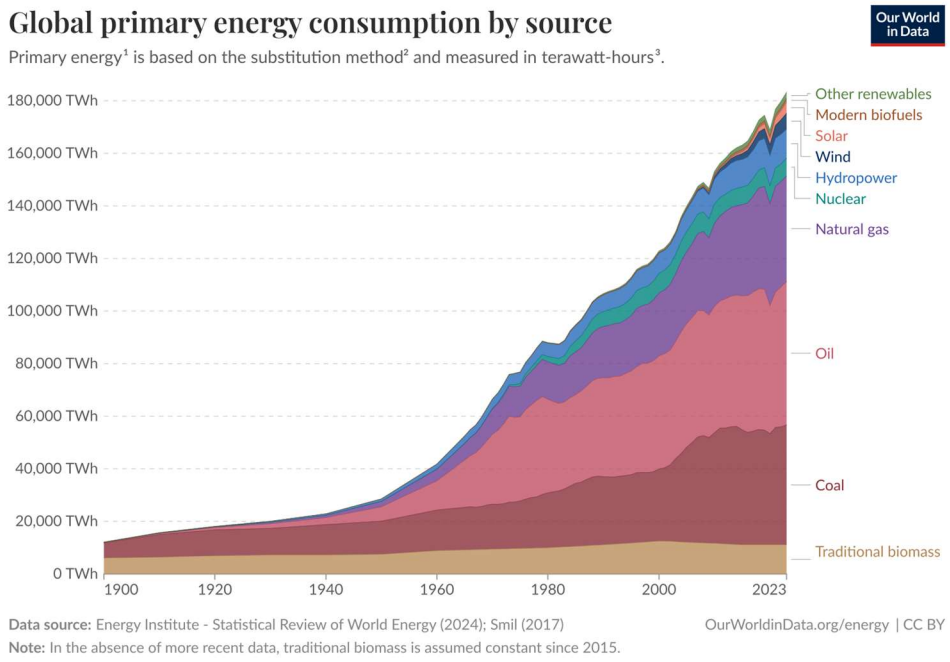

Figure 7: Breakdown of Global Energy Consumption.[18]

Lithium-ion Batteries (LIB) dominate the energy storage market with widespread applications in phones, computers, electric tools, and electric vehicles.[20] While major advancements have been made to allow for improved cycling and battery life, there are still safety concerns and optimizations needed with power density. As a result, research has expanded into alternative aqueous ion battery technologies, including potassium-ion batteries (KIBs). KIBs are comparable to LIBs where K^+ ions are inserted into the negative electrode during charging and during discharging, the ions migrate back to the positive electrode (Figure 8). However, they offer advantages including non-toxic elements, increased stability, and the possibility of higher power density coming from the difference in redox potentials ($-3.040\ V\ vs\ SHE$ for Li and $= -2.936\ V\ vs\ SHE$ for K).[21]

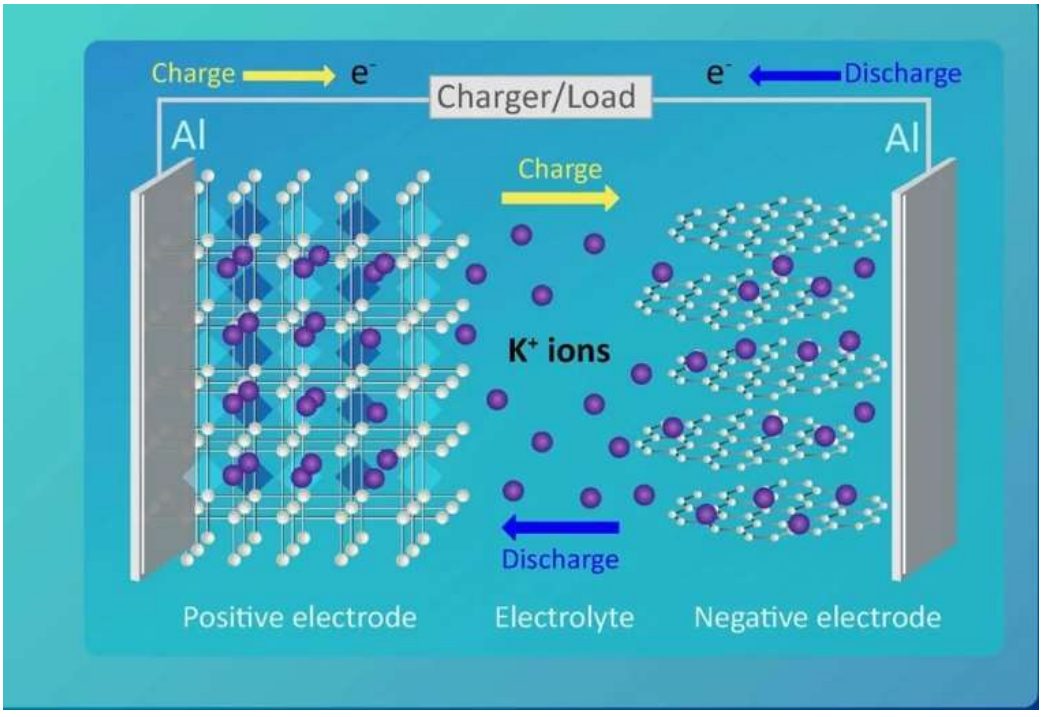

Figure 8: Schematic of KIB

Schematic of an aqueous potassium-ion battery (KIB).[22]

As potassium-ion batteries are explored as a promising addition to the aqueous ion battery field, system optimization is necessary to accommodate the specific chemistry of KIBs, including the development of ideal electrode materials. One promising class of materials is the hexacyanometallates, which are being actively researched as cathode candidates due to their wide range of electrochemical properties.[23] The versatility in the choice of metals incorporated into the lattice enables the tuning of material characteristics, offering opportunities to optimize performance for specific battery chemistries. The generic formula is given in Equation 2 where **A** is the guest cation (Li, Na, K, Mg, or Ca), $\boldsymbol{M_A}$ is an electrochemically involved transition metal (Fe, Mn, Co, Ni, or Cu), $\boldsymbol{M_B}$ is a second metal in the lattice, commonly Fe, which doesn't react.[23]

$$A_x M_A [M_B (CN)_6]_y \tag{2}$$

The structure of a generic hexacyanometallate is shown in Figure 9A, where the lattice adopts a face-centered cubic arrangement with an overall octahedral geometry.[24] One advantage of this lattice structure is its inherent flexibility, which facilitates the insertion and removal of ions during battery operation.

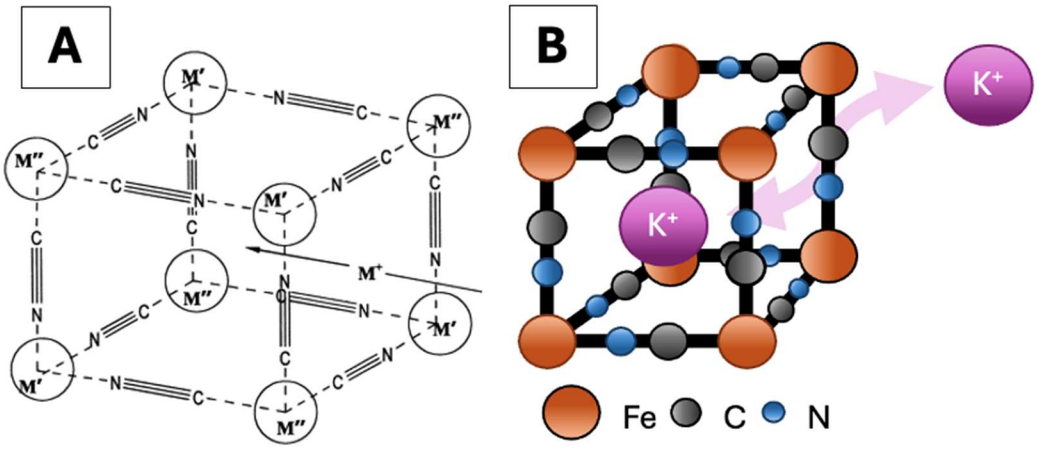

Figure 9: Structure of Hexacyanometallates and Prussian Blue Lattice

A) Generic structure of a hexacyanometallate lattice (Equation 2), and B) The specific structure of Prussian Blue, a hexacyanometallate, illustrating how K^+ ions interact with the cubic structure.[23]

Within the hexacyanometallate family, Prussian Blue analogs serve as a strong example of the broad range of possible electrochemical reactivity.[25] In the basic Prussian Blue structure, both metal sites in the lattice are occupied by iron; however, substituting the M_A iron with different transition metals allows the structural and electrochemical properties to be tuned, making these materials adaptable for a variety of applications.[10]

Prussian Blue (PB) is an electrochromic material, meaning it undergoes a reversible color change when an electric field is present or applied.[26] This color change is driven by variations in the oxidation states of iron within the structure. The three most common states are Prussian Brown (PX), Prussian Blue (PB), and Prussian White (PW), with their corresponding formulas shown in Equations 3–5. Additionally, Prussian Yellow and Prussian Green can form as intermediate states, though they are less commonly observed.

$$Fe^{3+}[Fe^{3+}(CN)_6]^0\ (PX) \quad (3)$$

$$Fe^{3+}[Fe^{2+}(CN)_6]^-\ (PB) \quad (4)$$

$$Fe^{2+}[Fe^{2+}(CN)_6]^{2-}\ (PW) \quad (5)$$

Prussian Blue (PB) was first synthesized as a dye in 1704 and later received increased attention in the late 20th and early 21st centuries for its potential in battery applications.[27] PB represents the most stable and commonly observed state within its oxidation series and can be easily deposited as a thin film. Due to its open framework in the lattice, the films are suitable for holding positive ions on a large scale at low costs.[28] In battery systems, PB undergoes a phase transition to Prussian White (PW), a process that is coupled with the insertion and removal of cations during charging and discharging (Equation 6). During the phase transition, one of the irons in Prussian Blue is reduced resulting in Prussian White. As the iron sites are reduced, positively charged ions (K^+) move into the film to balance charge. The filled lattice is visibly clear, giving it the PW name and demonstrating PB's electrochromaticity.

$$KFe^{3+}[Fe^{2+}(CN)_6]\ (PB) + e^- \leftrightarrow K_2Fe^{2+}[Fe^{2+}(CN)_6](PW) \quad (6)$$

Prussian White is also referred to as *Everitt's Salt* (ES). Studies have shown that the PB to ES conversion involves an electron-hopping mechanism, with the reduction reaction initiating at the electrode/film interface. As a result, ion transport is expected to be faster than electron transport.[25] Variations on this mechanism depend on the electrolyte environment and characteristics of the intercalating ion.[29,30] While current literature has extensively examined the transport of ions into and out of the PB lattice, the detailed mechanism of ion transfer remains less understood.

One of the key advantages of Prussian Blue is its ability to be electrodeposited from solution to form a lattice-structured thin film. A study details the deposition process, electrochemical analysis of ion intercalation, and the structural characterization through surface analysis techniques.[31] Figure 10 illustrates that the peaks associated with the reduction of PB to PW are reversible in nature. However, the peak behavior varies depending on the quality of the gold electrode and the local electrochemical environment.

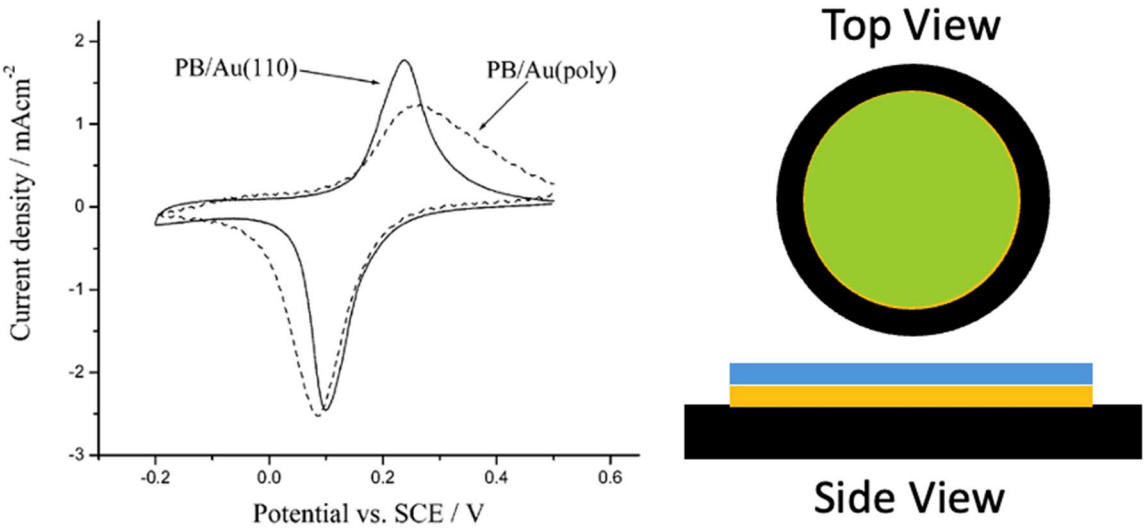

Figure 10: CV and Pictorial Representation of Electrodeposited PB film

Literature graph showing CVs of electrodeposited epitaxial Prussian Blue (PB) film on Au(110) compared to polycrystalline Au (left). A schematic (right) illustrates the top and side views of the polycrystalline Au dot electrode and the Prussian Blue thin film following electrodeposition.[31]

While literature on other PB analogs (where $M_A \neq M_B$) has explored the effect of deposition time on the resulting film structure, this research has not yet been extended to Fe-Fe PB lattice structures.[32] Thin films are commonly used as model systems because they enable the decoupling of transport and kinetic limitations in electrochemical studies.

For this Prussian Blue model system, the kinetic analysis is based on similar electrochemical features seen for PB/PW redox when compared to adsorption peaks and isotherms from Cu and H adsorption.[17,33] Kuo et al. demonstrated for hydrogen absorption onto a platinum working electrode that the apparent rate constant can be determined across a range of scan rates, which can then be fitted to provide an overall exchange rate (Equation 7).

$$k_{app} = \frac{J(E)}{Q^*} \tag{7}$$

The apparent rate of interfacial ion transfer (k_{app}) is determined by the current density as a function of potential and the charge density (Q^*). The objective is to use this value to calculate the exchange rate (k_0) for a species at a given steady state. The paper employs Butler-Volmer-like kinetics to determine k_0) and fit the electrochemical data, as outlined in Equation 8.[33]

$$k_{app} = k_o\big(\theta(1-\theta)\big)^{\alpha}\left[\exp\left(\frac{\alpha e\xi}{k_bT}\right) - \exp\left(\frac{-(1-\alpha)e\xi}{k_bT}\right)\right] \tag{8}$$

In the equation above, θ represents the coverage of absorbed species on the electrochemical substrate, ξ is defined as the driving force where $\xi = E - E_{eq}$, and α, e, k_b, and T are the transfer coefficient, elementary charge of an electron, Boltzmann constant, and temperature respectively. This model applies to systems where adsorption occurs on a fixed number of active sites at the polarized interface, as detailed for proton adsorption on Pt(111) by Kuo et al.[33,42] and Cu^{2+} adsorption at Au(111) by Thurman et al.[17]

Similar electrochemical data from $CuSO_4$ absorption/desorption and the PB/PW phase transition led to the question of whether adsorption can be used as a model for ion insertion into a lattice. To adapt Equations 7 and 8 for the PB model system, $Q^* = Q^*_{K+}$ will represent the

charge density held within the lattice and $\theta = Q_{K+}$ where the definition of coverage is more appropriate if we use the content of K^+ ions in PB.

Although the mechanisms of adsorption and insertion may not inherently appear the same, similar electrochemical responses prompted an investigation into whether the Kuo and Suntivich model can be applied to a broader range of electrochemical systems. The reversible nature of the PB/PW phase transition suggests that this approach could be a promising method for studying the phenomenon. However, the system is constrained by limited understanding of the ion dynamics once inserted into the lattice. In an adsorption system, ions typically occupy a fixed number of active sites; in contrast, within the lattice, more than a single layer of ions can be inserted, even in thin films. Regardless of the observed mechanism at the interface, the diffusion of ions within the PB lattice may introduce complexities that are not accounted for by this model.

2.2. The Research Question

In this chapter, the research aimed to address how cations interact with the electrode/electrolyte interface during ion transfer, particularly when investigating the PB/PW phase transition in various electrochemical environments. The hypothesis is that the insertion mechanism of K^+ into a Prussian Blue thin film will exhibit kinetics similar to those of an adsorption reaction, where ions adsorb onto an active substrate when thin films are used as a model system. However, complications arising from the dynamic interactions between cations and the lattice may require modifications when fitting insertion data to Equation 8. The significance of this work lies not only in studying the composition of Prussian Blue thin films but also in understanding the mechanism behind phase transitions, which can provide valuable insights into interfacial ion transfer in insertion/removal electrochemical systems and contribute to the development of sustainable energy storage devices.

2.3 Results and Discussion

2.3.1: Understanding the Interaction of PB Thin Films and Cation Cycling

This thesis aims to investigate the nature of interfacial ion transfer in systems involving lattice structures and mobile cations. To effectively study the interfacial reactions, it is important to decouple the contributions from diffusion and kinetic limitations. Since K^+ ions already exhibit relatively fast diffusion, particularly in the presence of KCl as a supporting electrolyte, one strategy to reduce diffusion-related effects is the use of thin films. With thin films, as K^+ is inserted into the PB lattice, fewer ions are required from the bulk solution, and those that are needed are readily available near the interface. To explore the relationship between integrated charge and deposition times for the PB thin films, a set of electrodepositions was carried out. Prussian Blue (PB) films were electrodeposited by applying +0.3 V vs SCE to cleaned Au surface in 5 mM $K_3Fe(CN)_6$, 5 mM $Fe(NO_3)_3$, with 0.25 M KCl as a supporting electrolyte.[31] For each film, cyclic voltammetry was used to find the insertion and the removal peaks, which were integrated to find the charge, proportional or the number of K^+ ions involved in the redox process. Figure 11 displays the integrated charge as a function of electrodeposition time.

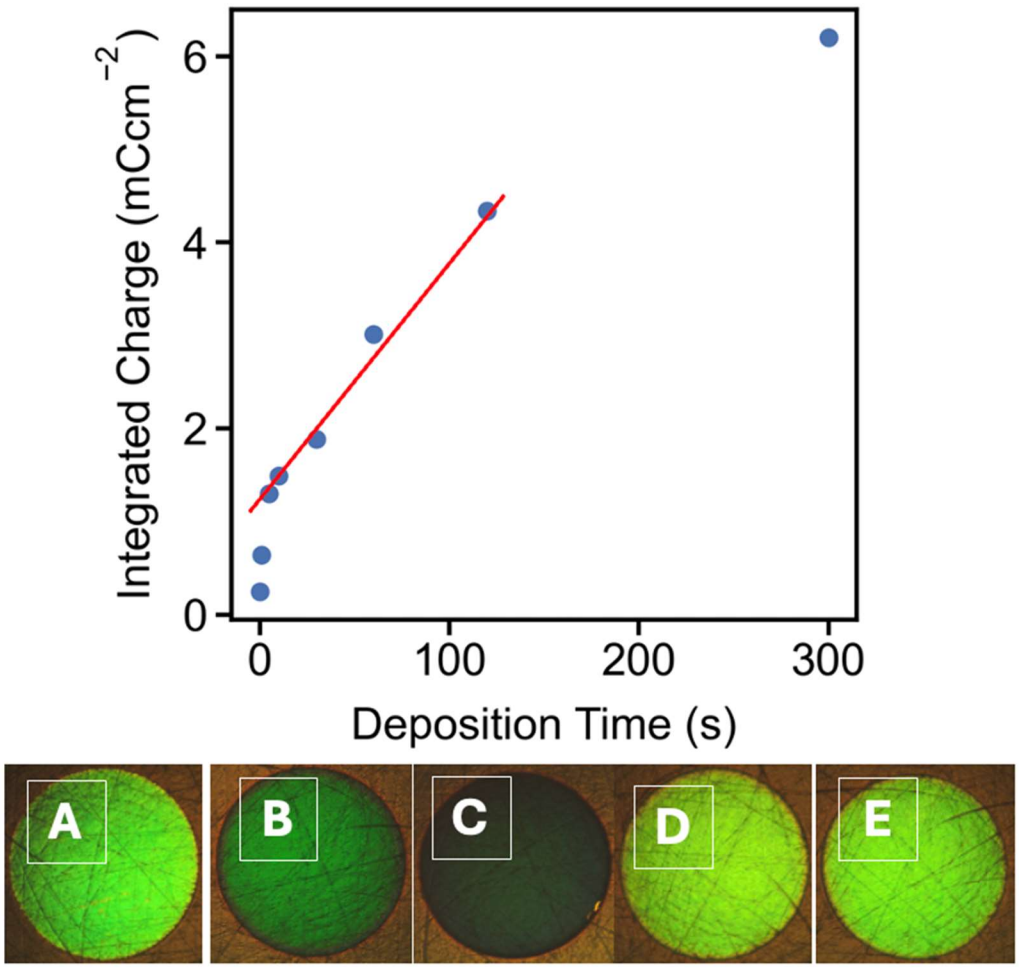

Figure 11: PB Thin Films Characteristic with Deposition Time

[Top] Integrated charge as a function of Prussian Blue deposition time, with a linear region identified (red line). [Bottom] Optical microscope images of electrodeposited Prussian Blue thin films at various deposition times: A) 5 sec, B) 2 min, C) 5 min, D) 30 sec – before cycling, and E) 30 sec – after cycling.

Initially, a steep increase in the integrated charge was observed between 1 and 5 seconds, followed by a linear region from 5 seconds to 2 minutes of deposition time. Beyond this linear region, the curve begins to bend slightly downward, indicating that the deposition time and integrated charge are no longer directly proportional. The goal of identifying a linear thin film region where the integration charge proportional is to deposition time is the ability to create uniform and reproducible PB thin films that can be developed for electrochemical testing.

Linearity ensures that minor variations in deposition time will not significantly affect the film's electrochemical behavior. For instance, if the potentiostat applies 31 seconds of deposition instead of 30 seconds, the resulting film would not be significantly thicker, and the same characteristics would be observed.

To find the optimal electrodeposition times for a uniform and reproducible thin film, the optical microscope was used to examine the PB working electrode after the deposition. Figure 11 A-D shows examples of PB thin films deposited onto the Au substrate (5 seconds, 2 minutes, 5 minutes, and 30 seconds). As the deposition time increases, the color of the film darkens, indicating a thicker film. This observation is supported by the increasing integrated charge; as the deposition time increases, the film becomes darker and the number of K^+ inserted rises. A 30-second deposition falls in the middle of the linear region, a sweet spot for uniform and reproducible films. Between Figure 11D and 11E, the PB thin film underwent a series of cyclic voltammograms with K^+ inserted and removed from the film. The film showed consistent coverage across the Au electrode both before and after cycling, suggesting that it remains uniform even after electrochemical testing.

Electrochemical Impedance Spectroscopy (EIS) was used to verify the stability of the electrodeposited films. EIS measurements are performed by applying a small sinusoidal voltage (PEIS) or current (GEIS) to a system at steady state and analyzing the resulting current or voltage response in the frequency domain. The impedance is represented in the complex plane with real and imaginary components corresponding to resistive and capacitive elements of the system. Resistors are purely in the real plane and the value of impedance is equal to the resistance. On the other hand, capacitors, are given as complex numbers (i) and lay in the imaginary plane. The theory behind EIS is that electrochemical cells can be modeled as AC

circuits with resistors and capacitors representing parts of the electrochemical process. Specifically, a simplified Randle's circuit is often used to describe an electrochemical cell (Figure 12).[34]

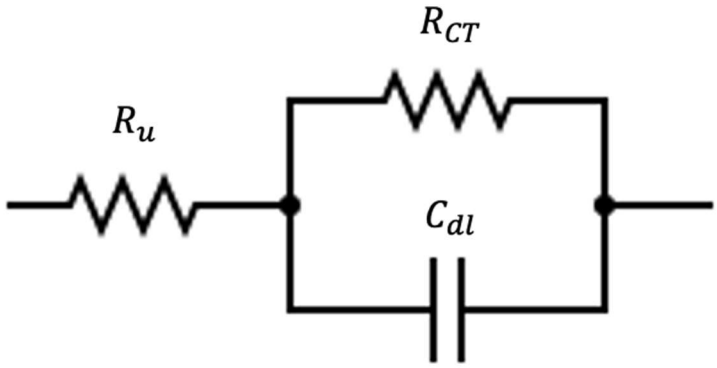

Figure 12: Circuit Diagram of Simplified Randles Circuit

An equivalent circuit diagram showing a simplified Randles circuit which is a model for the circuit elements of an electrochemical cell.

A Randles circuit consists of two resistors and one capacitor, each of which is assigned a component of an electrochemical process at an interface. The uncompensated resistance (R_u) arises from the inherent electrolyte resistance to a redox process and is in series with the parallel electrode double-layer capacitance (C_{dl}) and charge transfer resistance (R_{CT}). In the case of PB thin films, the solution resistance is particularly relevant, as we are interested in probing the interaction between the film and the electrolyte at the interface.

PEIS was utilized to identify if PB films are stable throughout the electrochemical analysis. This technique allows us to track changes in the interfacial properties over time. A variation in R_u during repeated measurements may indicate changes in the PB/electrolyte interface, such as film degradation or restructuring. The impedance data collected from PEIS is typically represented using a Nyquist plot, where the imaginary and real components are plotted together.

From this plot, the uncompensated resistance can be extrapolated, providing insight into the interfacial dynamics and overall system stability. Figure 13 shows PEIS traces taken across different conditions of a PB film.

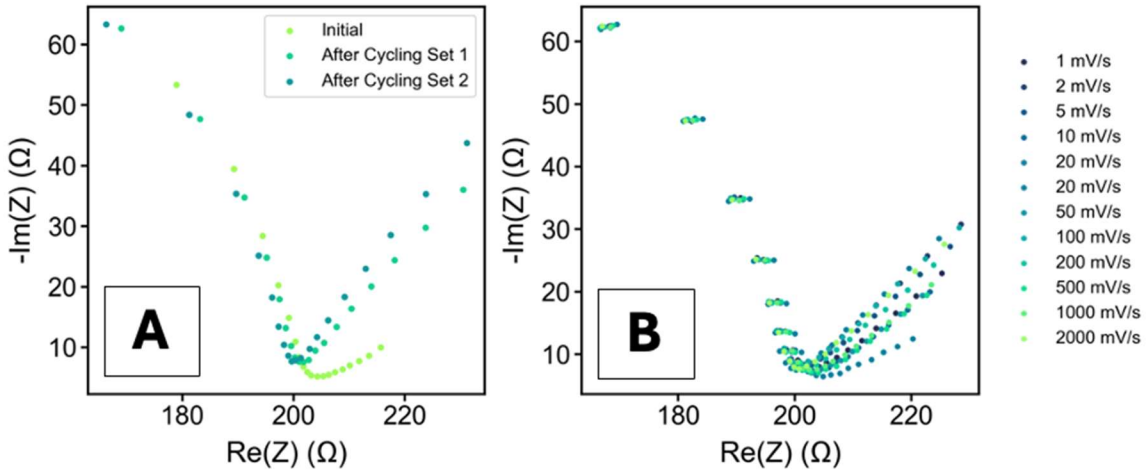

Figure 13: EIS on PB Thin Films

Nyquist plots from Potentio Electrochemical Impedance Spectroscopy (PEIS) measurements conducted from 1 MHz to 1 kHz, showing A) the stability of Prussian Blue thin films through cycling, and B) consistent resistance across different cycling scan rates.

Figure 13A shows that a PB film can be stable across multiple sets of electrochemical cycling experiments. The value of R_u is taken from the point where the capacitive contribution is the smallest.[34] The imaginary component never approaches zero, reaching a minimum of 8 Ω, indicating a persistent capacitive element. Initially, the solution resistance was 204 Ω, and after cycling experiments, it slightly decreased to 201 Ω and stayed constant. The PEIS is taken at +0.7 V vs SCE, a potential where PB does not readily accept K^+, however, there may be some inherent electrostatic attraction between the two creating an electrochemical double layer. The value of resistance remaining constant across sets of cycling for a PB film indicates that the film structure and interaction with the electrolyte remain consistent, even as the potential is applied.

Similarly, Figure 13B shows that the resistance remains constant, remaining around 201 Ω, across 12 scan rates. If the resistance had changed between a slower (1 mV/s) and a faster (2000 mV/s) scan rate, it could suggest the film structure changes based on the speed of the cycling of K^+ ions into and out of the film. However, since the impedance response remains constant, this implies the PB structural integrity is maintained, regardless of the rate of K^+ ion insertion and removal.

The electrochemical technique, cyclic voltammetry (CV), has been referenced above and is crucial for understanding the electrochemical characteristics of a redox reaction. In a CV experiment, a defined potential window is applied to an electrochemical system, and the resulting current is measured. Potential (E), measured in vols (1 V = 1 J/C), is the energy needed to move charge in a system. Current, measured in amperes (1 A = 1 C/s), is the rate at which the reaction is happening. The magnitude of the current corresponds to the extent of the reaction occurring at a given potential, and the sign denotes if the reaction is a negative reduction current (loss of electrons) or a positive oxidation current (gaining electrons). Current is often normalized to the electrode surface area and expressed as current density (*J*) as a way to compare values across systems. CVs are particularly valuable for studying redox-active species, as distinct peaks appear when a compound undergoes reduction or oxidation. Figure 14 displays the cyclic voltammograms of the PB system recorded at various scan rates, highlighting its redox behavior under different electrochemical conditions.

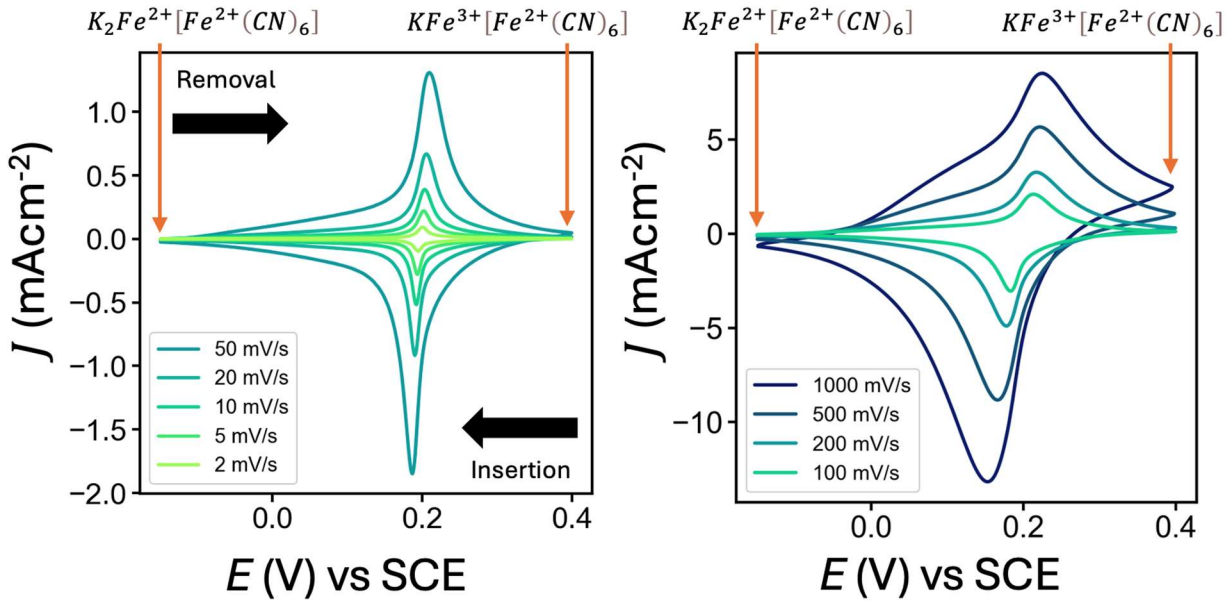

Figure 14: CVs of PB Thin Films at Different Scan Rate

Cyclic voltammograms taken in 1 M KNO_3 recorded at low (left) and high (right) scan rates, illustrating the current–potential response during K^+ ion insertion and removal associated with the Prussian Blue (PB) to Prussian White (PW) transitions. The orange arrows point at the potential for which we expect the corresponding compound to exist.

For the PB films, CVs begin at 0.4 V vs SCE, where the PB film is vacant of any potassium ions. As the potential is swept negatively, PB is reduced to PW and K^+ ions are inserted to help balance the lattice charge. At the vertex of -0.15 V vs SCE, the film is said to be saturated with K^+, as the current indicates a redox reaction is no longer underway. On the positive sweep, K^+ is removed as PW is oxidized to PB. The peaks in the voltammogram correspond to the potentials where the redox reactions are most active, and where the highest flux of K^+ ions cross the electrochemical double layer and enters or exits the PB lattice.

Figure 14 displays two sets of CV curves: slow scan rates (left) and fast scan rates (right). At slow scan rates, the redox peaks are sharp and symmetrical, indicating a highly reversible process. The symmetry of the reduction and oxidation peaks suggests that the same potential (+0.2 V vs SCE) is required to reduce PB to PW as to oxidize PW back to PB, further reinforcing

the reversibility of the system. At faster scan rates, however, the peaks broaden and become less symmetric, with a noticeable separation between the insertion and removal peaks. The reduction peak shifts to more negative potentials, indicating that greater energy is needed to insert K^+ ions at high scan rates. A shoulder peak appears during the oxidation at 1000 mV/s, suggesting a deviation in the K^+ removal mechanism. The K^+ ions favor being in the electrolyte rather than within the PB lattice at more positive potentials due to the iron atoms transitioning to a higher oxidation state and the lattice adopting an overall more positive charge.

The hypothesis is that at high scan rates, K^+ ions don't have sufficient time to diffuse from the surface to deeper into the PB film. The energy the energy to pull the ions back into the electrolyte is lower when the K^+ ions are near the top of the film. However, fully removing K^+ from the lattice requires the same applied potential, which explains why the peak current remains at +0.2 V vs SCE, even as the peak has broadened over a range of potentials.

2.3.2: Understanding the Effect of Electrolyte Concentration on Insertion Mechanism

Electrolytes with varying concentrations were employed to supply cations to the system to gain a deeper understanding of the interaction of the PB lattice and K^+. Figure 15 presents the CV traces for differing $[K^+]$ in KNO_3 electrolytes.

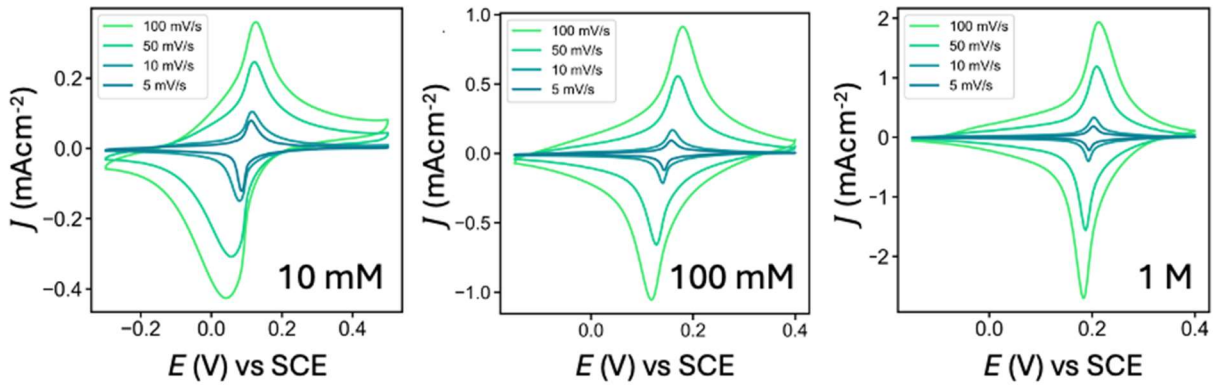

Figure 15: CVs of PB Thin Films at Different [K^+]

Cyclic voltammetry responses for the insertion and removal of K^+ ions into Prussian Blue thin films at varying concentrations of KNO_3. Measurements were performed using the electrochemical setup described in Figure 27.

Distinct changes in the shape of the voltammograms are observed across the three different [K^+]. At 1 M and 100 mM, symmetric adsorption traces are present, indicative of a reversible insertion and removal process as described above. In contrast, at 10 mM, the decay of the peaks is broader and less uniform. Additionally, the magnitude of peak current ranges from 0.4 mA cm^{-2} at 10 mM to 2 mA cm^{-2} at 1 M. Interestingly, as will be discussed quantitively later, the charge held within the PB lattices remains approximately constant across the different concentrations.

The variation in voltammogram shape at 10 mM is attributed to diffusion limitations within the electrolyte since the concentration of K^+ ions within the PB film is constant as seen in Figure 16. With a lower concentration, there is a limited amount of K^+ ions at the surface. As K^+ ions are inserted into the lattice, the surface layer becomes depleted, and the electrolyte cannot readily replenish these ions. Subsequent K^+ insertion requires diffusion from deeper within the bulk solution, demanding more energy and resulting in a broader, lower-current peak. For the 1 M electrolyte, the PB/electrolyte interface is saturated with K^+, and the insertion is only limited by

the vacant sites within the PB film, and not by ion transport from the bulk solution to the interface.

Differences in the magnitude of *J* can also attributed to K^+ ion diffusion. At the fastest scan rates, peak currents differ significantly across concentrations. However, as you get to 5 mV/s, the differences seem to diminish. Due to the difference in scaling in Figure 15, it is more difficult to see, but Figure 16 highlights how *J* becomes consistent at slow scan rates. Under low concentrations and fast scan rate conditions, the system is pushing K^+ ions in and out of the PB lattice, without sufficient time to equilibrate. The limited number of K^+ at the surface requires more potential and a broader window for the insertion mechanism is seen. However, at slower scan rates, the cell has time to equilibrate with the changing electrode potential, enabling K^+ ions to diffuse to the interface from the bulk solution. In high-concentration electrolytes, diffusion is not a limitation, and the magnitude of current is governed by the number of K^+ ions in the lattice, explaining why the value of *J* is similar at these slower scan rates.

A noticeable shift in the peak potentials across the different concentrations of K^+ was observed. Figure 16 shows the slowest scan rate of each concentration, side by side, to highlight the change in peak position.

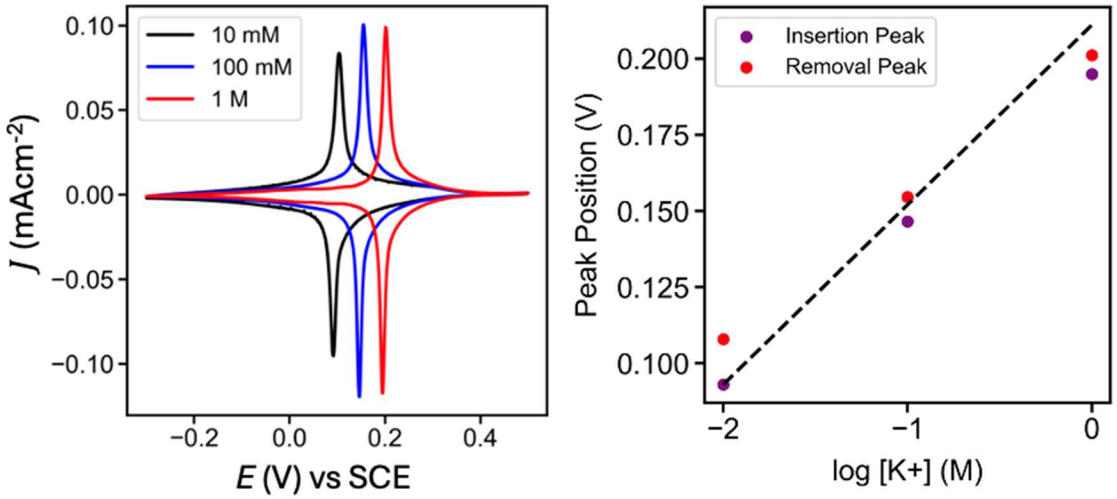

Figure 16: Comparing Peak Potential Across Varying [K+]

A) Cyclic voltammetry (CV) traces at 2 mV/s showing how the insertion/removal peaks shift with varying [K^+]. B) Peak positions from Figure 15 plotted as a linear function of log[K^+], behaving close to a Nernstian system (dashed line).

In the left panel of Figure 16, the slowest scan rate is plotted for each electrolyte concentration. The symmetric redox peaks systematically shift to higher potentials as the amount of K^+ in solution increases. When the peak potentials corresponding to the insertion and the removal were plotted against log[K^+], a linear relationship was seen. The slopes for the insertion peaks and the removal peaks were 51 mV/dec and 46 mV/dec, respectively, which are in close agreement with the Nernstian slope of 59 mV/dec, seen on the right panel.[35]

According to the Nernst equation, the electrode potential of a redox reaction depends on the concentration of the redox species. For a Nernstian one-electron reaction, the potential shifts by approximately 59 mV per one tenfold change in the concentration. The redox reaction converts the oxidation state of the iron within the PB lattice, and the potentiostat measures the charge compensation, or K^+ ions passing through the double layer. Therefore, a shift in the potential is expected when the [K^+] is varied.

The measured slopes have a slight deviation from the ideal value of 59 mV/dec, likely due to the variations in electrolyte ionic strength. Normalizing the ionic strength of an electrolyte ensures that a consistent number of charged ions are available in the solution, which supports ion transport to and from the electroactive site. In this experiment, the ionic strength was not normalized, which potentially affects the diffusion of K^+ ions to and from the PB surface. As a result, the peak shifting does not exactly follow the Nernstian shifting since the total ion concentration is not the same, however, the values are still in close agreement.

The magnitude of current density remains approximately equal across the different [K^+] at the slowest scan rate. For kinetic analysis, it is essential to determine the amount of charge transferred during a redox cycle, as this value is proportional to the number of K^+ ions held in the PB lattice. CVs at 2 mV/s were precisely integrated to calculate the charge passed. Figure 17 displays an example CV used for this determination of charge.

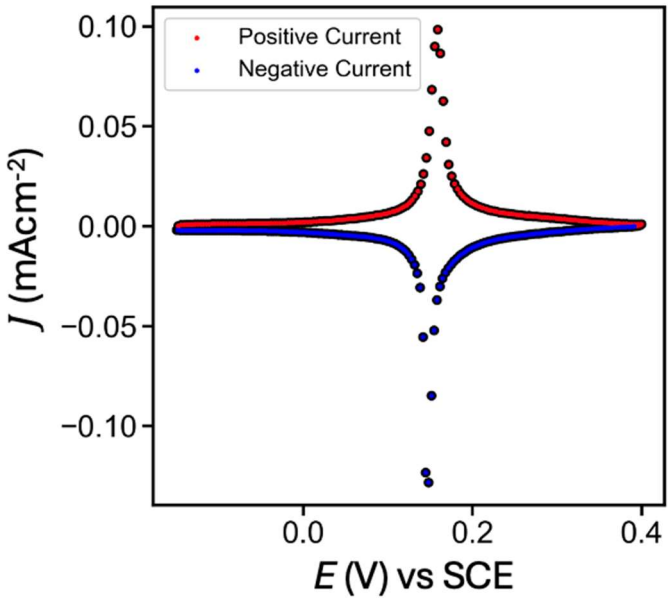

Figure 17: Example of Integrated CV for Charge Calculation

Cyclic voltammogram recorded at the slowest scan rate (2 mV/s), with positive and negative current regions differentiated to indicate the areas used for charge capacity integration.

For a lattice-based system, such as PB, the insertion and removal of K^+ ions are reversible expected to be reversible, which was shown in previous figures. Provided that the CV response and PB film structure remains consistent across multiple cycles, the charge insertion should be equal to the charge removed. In other words, the number of K^+ ions inserted should be equal to the number of K^+ removed. Table 1 reports the measured charge densities for each concentration of electrolyte.

Table 1: Measured Charge Capacities

Reported measured charge capacities for K^+ ion insertion and removal peaks at varying [K^+] concentrations. Values represent averages with standard deviations calculated from triplicate measurements.

[K+]	Average Insertion Charge Capacity (mC)	Average Removal Charge Capacity (mC)
10 mM	0.18 ± 0.03	0.17 ± 0.03
100 mM	0.17 ± 0.03	0.16 ± 0.04
1 M	0.156 ± 0.007	0.16 ± 0.01

Each reported value represents the average of triplicate measurements with an associated standard deviation. As expected, the integrated charges for K^+ insertion and removal are within experimental error for all three [K^+]. Furthermore, the measured charge capacities for the varying concentrations fall within the standard deviation of each other. These findings support the reversibility of the redox process and the indication that each PB film can accommodate the same number of K^+ ions within its lattice, regardless of electrolyte concentration.

The consistent charge capacity across electrolyte concentrations, despite observable changes in CV traces, suggests a different mechanism of K^+ interacting with the PB film. The peak current (i_p) for the removal and insertion was found and plotted logarithmically against the

square root of the scan rate (ν) to evaluate the nature of these charge transport processes (Figure 18).

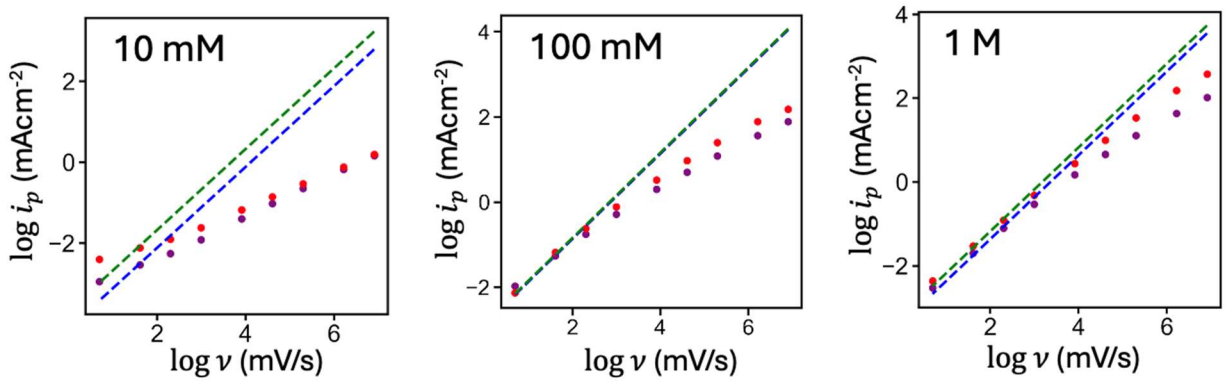

Figure 18: Mechanism Fitting of Insertion and Removal of K^+

Log-scale plot of peak current versus the scan rate for various [K^+] insertion (purple) and removal (red) peaks. Linear fits based on an adsorption-controlled mechanism using the Randles-Sevcik equation (Equation 9) are shown in blue (insertion) and green (removal).

Plotting the log of peak current against the log of square root scan rate is based on the Randles-Sevcik theory (Equation 9).[34] According to this model, the resulting plot provides insight into the rate-limiting mechanism of the redox process. A slope of 0.5 indicates complete diffusion, a slope of 1 indicates complete adsorption control, and a value in between implies the reaction is a combination of the two. In Figure 18, linear fits for the insertion (purple) and removal (red) data were generated with a slope of 1 to isolate the regions where adsorption dominates. As the concentration of K^+ increases, there is less deviation from the ideal fit lines. One explanation for the curvature observed at high scan rates is the increasing impact of diffusion limitations, which cause the peak current to fall below the adsorption-controlled line.

$$i_p = 0.4463nFAC * \sqrt{\frac{nF\nu D}{RT}} \quad (9)$$

The Randles-Sevcik equation is given by the number of electrons in the reaction (n), Faraday's constant (F), surface area of the working electrode (A), concentration (C), the gas constant (R), temperature (T), the diffusion coefficient (D), and scan rate (ν). Table 2 displays parameters from the Randles-Sevcik fitting in Figure 18. The R^2 values for the linear fits with fixed slope (adsorption model) are reported for each concentration, alongside the number of scan rates included in the fit. Additionally, an unconstrained linear regression was conducted to identify if the slope was dictated by a different transport mechanism.

Table 2: Fitting Parameters for Mechanisms of K^+ Insertion and Removal

Fit parameters for the insertion and removal of K^+ ions at various concentrations. The number of scan rates used for an adsorption fit with a slope of 1 (Figure18) is reported, along with the R^2 value. Additionally, the slope of a linear fit based on the Randles-Sevcik equation (Equation 9), including all points, is also provided.

[K^+]		**Valid Points in Absorption Fit**	**R^2 value of Absorption Fit**	**Average Slope of log i_p vs log $\nu^{0.5}$**
10 mM	Insertion	None	N/A	0.43
	Removal	None	N/A	0.51
100 mM	Insertion	3	0.896	0.67
	Removal	3	0.991	0.71
1 M	Insertion	4	0.976	0.80
	Removal	4	0.983	0.73

As you increase [K^+], the number of scan rates that yield a valid linear fit assuming adsorption control (slope = 1) also increases. In the 10 mM electrolyte, no set of three scan rates can be adequately fit with a slope of 1.0, which is the minimum number required to perform a reliable linear regression. At 100 mM, the three lowest scan rates satisfy this criteria, and at 1 M, a fourth scan rate becomes valid under the adsorption-controlled assumption. This trend supports the observation from Figure 15, where the 10 mM CV traces exhibit diffusion limitations. This conclusion is further supported by the unconstrained linear fit slopes of 0.43 and 0.51. While

these values are not exactly at the theoretical diffusion-controlled slope of 0.5, they are close enough to suggest that diffusion is the dominant mechanism. Additionally, the negative R^2 values for the fixed-slope (adsorption) linear fit at 10 mM indicate that such a model is not appropriate in this case.

In contrast, the 100 mM and 1 M datasets show much stronger agreement with the adsorption model. The fixed-slope fits yield R^2 values greater than or equal to 0.90, indicating a strong linear correlation under the adsorption mechanism. Although the CVs imply an adsorption process due to the sharp, reversible peaks (Figure 15), the unconstrained slopes for the higher [K^+] electrolyte are not explained simply by Randles-Sevcik. The slopes are not 0.5 or 1 exactly, suggesting that the charge transfer mechanism at these higher [K^+] concentrations is not governed solely by either diffusion or adsorption but is instead a combination of the two. Notably, the slopes approach 1.0 as the electrolyte concentration increases, implying that adsorption becomes increasingly dominant relative to diffusion. However, deconvoluting the fractional contribution of each process is not possible from the data in Table 2 alone.

2.3.3: A Kinetic Analysis of Cation Insertion Mechanism

The foundation for our kinetic analysis is the adsorption-based model originally developed for H-adsorption on Pt(111) surfaces by Suntivich.[33] In this paper, the model they proposed is a Butler-Volmer type analysis with an added adsorption term as seen in Equation 8. We were interested to see if a similar treatment could be applied to interfacial K^+ transfer, which is different from H-adsorption in that K^+ cations are not adsorbing to the surface but instead inserting into a lattice. The big question in this subchapter aims to answer is if we can model insertion and removal interfacial ion transfer mechanism using an adsorption model. One

limitation is interworking of the K^+ and PB interaction are not explicitly known compared to the H- and Cu- adsorption process.[17]

To begin this analysis, we examine the K^+ content inserted into the PB film as a function of potential (Figure 19A). The potential required to achieve a specific K^+ content was extracted across a series of scan rates to compare the rate of K^+ insertion as a function of interfacial driving force. In Figure 19A, for the first 5 slow scan rates, the potential needed to achieve the same content of K^+ within the film remains constant. After the threshold of 50 mV/s, the slope starts to drop indicating that more cathodic potential is required to achieve the same number of ions inserted. The driving force, or the additional potential from that of the slowest scan, can be extracted and plotted against the apparent rate constant (Figure 19 B-D).

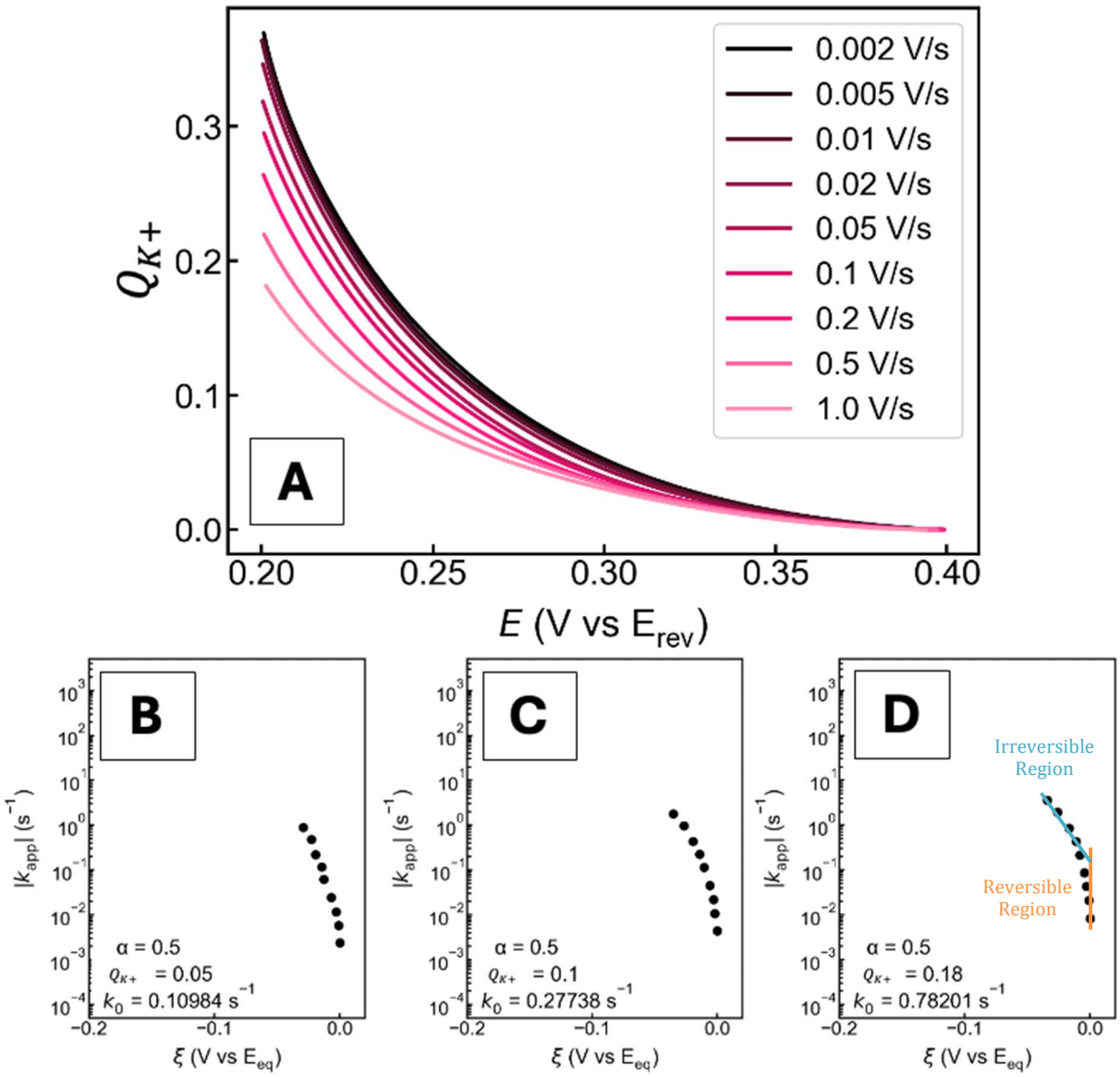

Figure 19: Kinetic Analysis of K^+ Insertion

A) Content of K^+ ions in the Prussian Blue thin film as a function of applied potential during ion insertion into the lattice. The bottom row shows the apparent rate as a function of driving force, used to extract the exchange frequency (Equation 8), for B) $Q_{K+} = 0.05$, C) $Q_{K+} = 0.1$, and D) $Q_{K+} = 0.18$.

Equation 8 was fit to current-voltage data to extract the apparent rate constant at zero-driving force, k_0, across a range of surface coverages. The parameter k_0 represents the exchange rate, or turnover frequency, at a given content of K^+ in the film. In practical terms, k_0 quantifies

the rate at which K^+ ions are inserted into and extracted from the PB lattice under a given driving force (defined by the potential or level of K^+ coverage).

The shape of the resulting curves offers insight into the transition between reversible and irreversible insertion regimes, showing as two distinct linear regions (Figure 19D). In the reversible region (orange), the driving force remains constant across different scan rates, indicating that equilibrium conditions are maintained. Conversely, the irreversible region (blue) emerges when the required driving force increases with the scan rate, signifying kinetic limitations. This behavior mirrors what is observed in cyclic voltammetry, where the cathodic (insertion) peak shifts to more negative potentials under non-equilibrium conditions. In Figure 19A, this transition is reflected as a reduced slope in the K^+ content versus potential plots indicating that a greater driving force is needed to achieve the same fractional insertion at higher scan rates.

To extract meaningful kinetic data, the scan rate must be increased sufficiently to drive the system out of equilibrium. This transition is more readily achieved at higher K^+ coverages, where a greater driving force is required to attain the same level of insertion compared to lower coverage regions. As a result, kinetic limitations become more pronounced, and the data begins to reflect deviations from equilibrium behavior.

The current fitting approach assumes that increasing the scan rate will shift the system into the irreversible regime, where the driving force continues to rise with scan rate. However, at lower coverages, the applied driving forces remain within the reversible region, preventing the acquisition of meaningful kinetic information. As scan rate increases, the applied overpotential becomes more negative, progressively pushing the system out of equilibrium. This trend

becomes more apparent at higher coverages (Figure 19D), where the resulting plots display greater curvature, indicating the onset of kinetic constraints.

This kinetic approach in Suntivich is based off a Butler-Volmer-like model (Equation 8) in which the transfer coefficient (α) is equal for the forward and reverse reaction based on the reversibility of the CV peaks, i.e. $\alpha = 0.5$. The transfer coefficient is an intrinsic property of a system which acts as symmetry factor between the activation energies for the reduction and oxidation reactions. The value of α significantly influences the slope of the kinetic fit as the system enters the irreversible region; a gradual curvature with a steep slope corresponds to a transfer coefficient near 0, whereas a more dramatic transition into the irreversible region with a lower slope is associated with an α value closer to 1. Figure 20 compares the kinetic model fit for $\alpha = 0.5$ to a fit for $\alpha = 0$, showing both fits alongside the experimental data.

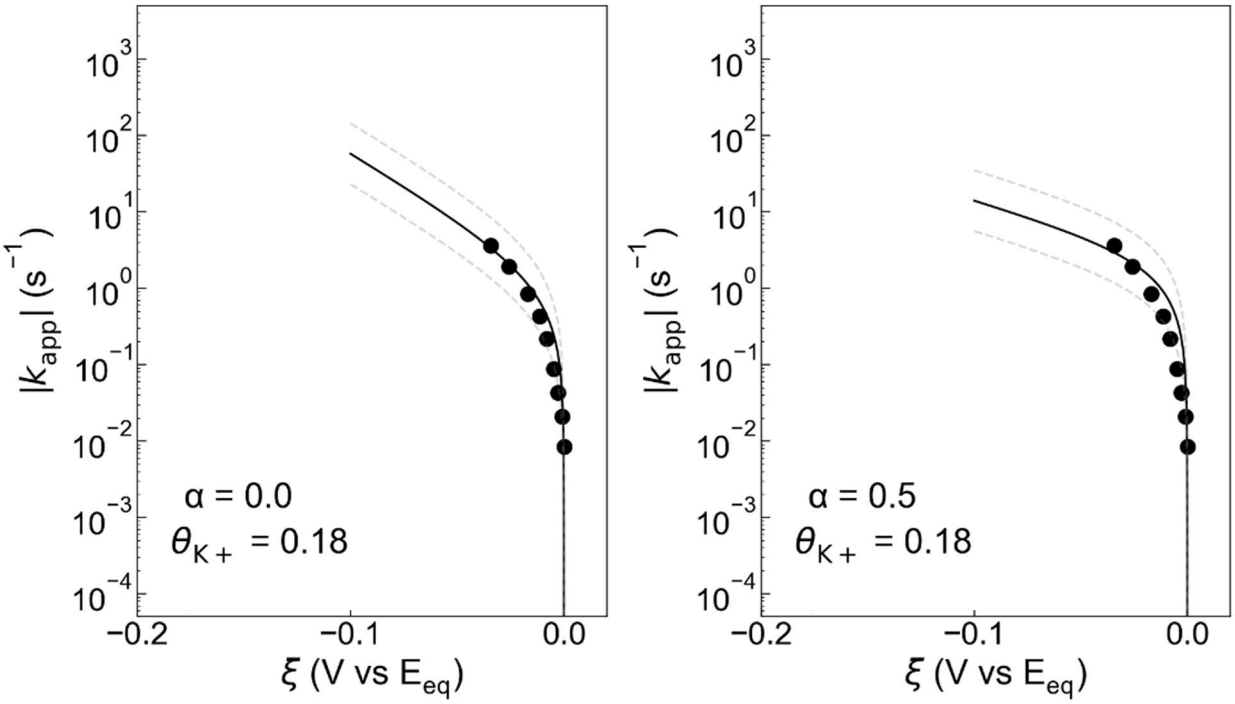

Figure 20: Kinetic Fitting of K+ Insertion

Comparison of the transfer coefficient (α), A) $\alpha = 0$ and B) $\alpha = 0.5$, fitting the apparent rate as a function of driving force, used to extract the exchange frequency (Equation 8). The dashed grey lines bracket the data in a range 0.5x and 2x times the fitting lines.

For a completely reversible reaction, $\alpha = 0.5$ denoting the energy for the reduction reaction is equally favorable to the oxidation reaction. Using $\alpha = 0.5$, the slope of the fit deviates from the data points, but when α is modified to be 0, the data more closely fits the kinetic model. This finding is not in agreement with a reversible insertion and removal of K^+ ions as seen in the cyclic voltammetry data. A transfer coefficient of 0 leads to an equation where the ion removal current contribution is independent of the potential applied (Equation 10). This suggests that all the applied potential is being used to maintain the PW phase. In other words, if the applied potential suddenly turned off that PW would readily convert to PB and kick out the K^+ ions inserted.

$$i = i_0\left[e^{\alpha f\eta} - e^{-(1-\alpha)f\eta}\right] = i_0[1 - e^{-f\eta}] \quad (10)$$

However, even the model in Equation 10 does not accurately describe the insertion mechanism for K^+ into a PB film. As seen in previous subchapters, cyclic voltammetry experiments performed in 1 M KNO_3 reveal characteristic peaks indicating that the system behaves reversibly with respect to the applied potential. The disagreement between the model fit and the experimental observations suggests that the Suntivich adsorption fitting is not valid for this insertion/removal system. One possible reason for this discrepancy may be an underlying mechanism within the PB film that remains poorly understood.

In the case of hydrogen adsorption onto platinum, the mechanism is well-established, with one hydrogen atom adsorbing to one platinum site.[36,42] However, for PB, the exact mechanism by which cations interact with the film is not yet known. While the data collected indicates the magnitude of K^+ ions crossing the double layer from the bulk electrolyte to the PB film interface, it does not provide information about the behavior of the ions once inside the film. One possibility is that diffusion of K^+ within the PB film plays a more significant role than recognized. Although the influence of solution-phase diffusion on the insertion rate has been demonstrated earlier, the internal diffusion within the film remains to be understood.

The data from the CVs coupled with the insertion coefficient of zero leads us to propose another model, seen in Equation 11.

$$i = i_0\left[e^{\alpha' f\eta} - e^{-\alpha f\eta}\right] \quad (11)$$

In this model, we propose that K^+ cycling behaves as an irreversible reaction, with the transfer coefficient for insertion (α) being asymmetric to that of removal (α'). In other words, the energy barrier for the insertion is not symmetric to the energy barrier for the removal. This model suggests that a phase transition occurs during the PB-to-PW conversion, resulting in

different ion insertion and removal dynamics depending on the phase of the film. Figure 20 shows that the transfer coefficient for the insertion of K^+, as PB is converted to PW, is equal to 0.

In the graphs above, the removal term had (1- α) the best fit as zero, however, in the way we propose the new model, the term can be modified to have α replace (1- α) and now it will be equal to 1. The interpretation of the data is the same, this is only changing the notation of how we display the transfer coefficient. Using the insertion information to inform the removal data, we can use similar fitting procedures to find the best transfer coefficient for the PW to PB conversion accompanied by the removal of K^+ ions. As mentioned earlier, fitting to Equation 11, we will assume that the transfer coefficients are asymmetric, and we can determine the transfer coefficient values independently for the removal and insertion. Figure 21 displays the change in the anodic potential needed to remove K^+ content from the PW phase of the lattice.

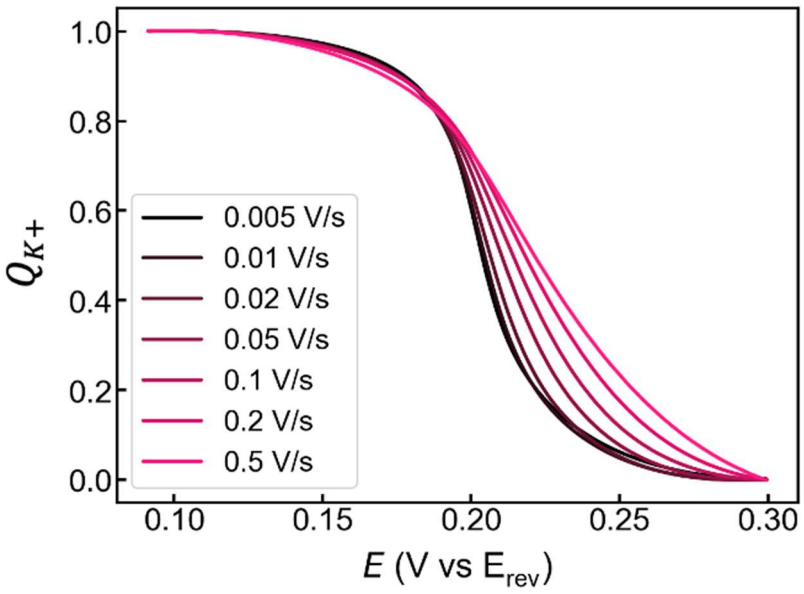

Figure 21: Kinetic Analysis of K^+ Removal

Content of K^+ ions in the Prussian White phase of a Prussian Blue thin film as a function of applied potential during ion removal out of the lattice.

As briefly mentioned previously, we hypothesize that the conversion from PB to PW and PW to PB result in different mechanisms. This accompanies a different active site for K^+ ions to removal from compared to where they were inserted. In Figure 21, the shape of the removal curves is different compared to the insertion curves in Figure 19A. In the case of removal, the process begins with a film saturated with K^+ ions. For all scan rates, the potential required to initiate oxidation and ion removal remains consistent until the film reaches a K^+ content of approximately 0.8. Beyond this point, the curves diverge, displaying an inversion and separation throughout the remainder of the removal process, before converging again as the K^+ content approaches zero.

To accurately model the insertion and removal of K^+ ions, kinetic fitting must be performed under comparable experimental conditions. For the insertion process, the K^+ content was approximately 0.18, and the data fit well using a transfer coefficient (α) of 1. To maintain consistency, the removal kinetics were analyzed at a similar K^+ content of 0.20. This enabled a direct comparison between the insertion and removal processes. The removal data was fit using a range of α' values to determine the most appropriate transfer coefficient for the ion extraction mechanism.

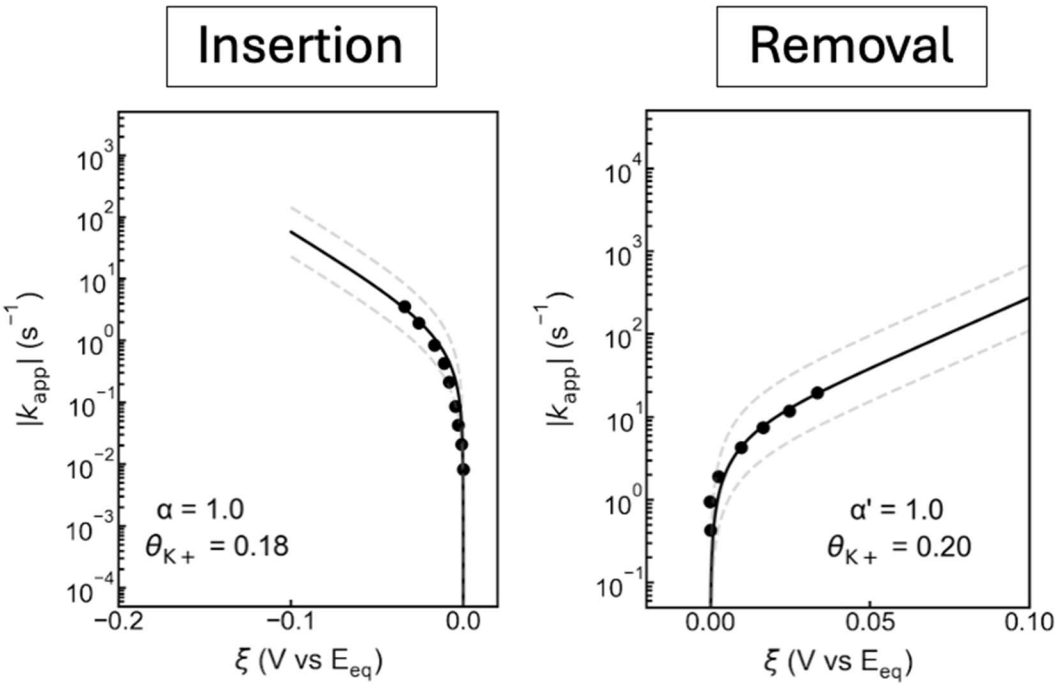

Figure 22: Insertion and Removal Transfer Coefficient Fitting

Comparison of the kinetic fitting for the insertion (left) and removal (right) of K+ ions. A set insertion transfer coefficient (α) of 1, fitting the apparent rate as a function of driving force, used to extract the exchange frequency according to the model in Equation 11. The dashed grey lines bracket the data in a range 0.5x and 2x times the fitting lines.

The results and comparison of the insertion and removal data are shown in Figure 22. The driving force for insertion is negative, while removal is positive, corresponding to a more cathodic or anodic potential, respectively, required to drive the reaction at higher scan rates. For both processes, a transfer coefficient of 1 for both α and α' provided the best fit to the data. This value suggests that the entire applied potential contributes to the progression from reactant to product phase, indicating that the system behaves irreversibly in both directions under the tested conditions. While further experimentation is needed to uncover the internal mechanisms responsible for this asymmetric barrier, these findings clearly demonstrate that a simple

adsorption model is insufficient to fully describe the insertion/removal behavior. This realization provides a strong foundation for future mechanistic investigations.

From this, a model can be constructed that incorporates both fitting parameters. If $\alpha = \alpha' = 1$, an asymmetric Butler Volmer-like model can be employed to describe the insertion and removal of K^+ ions in a Prussian Blue thin film. Future work can utilize this model to extract meaningful kinetic parameters, such as the exchange rate constant, which can help inform the design and optimization of energy storage systems.

2.2.4: Characterization of the Prussian Blue Film and the Effects of Cycling

One approach to examining the morphology of the PB film is to take SEM images. Scanning Electron Microscopy (SEM) characterization involves using a focused beam of electrons to scan a sample's surface and analyze the emitted signals to reveal surface morphology, composition, and other properties.[37] To investigate the influence of K^+ cycling on the PB film, two samples were prepared for SEM imaging: one that was freshly electrodeposited and had not undergone electrochemical testing (uncycled), and another that had completed a full sequence of electrochemical experiments (cycled). Figure 22 compares the two films at multiple magnifications.

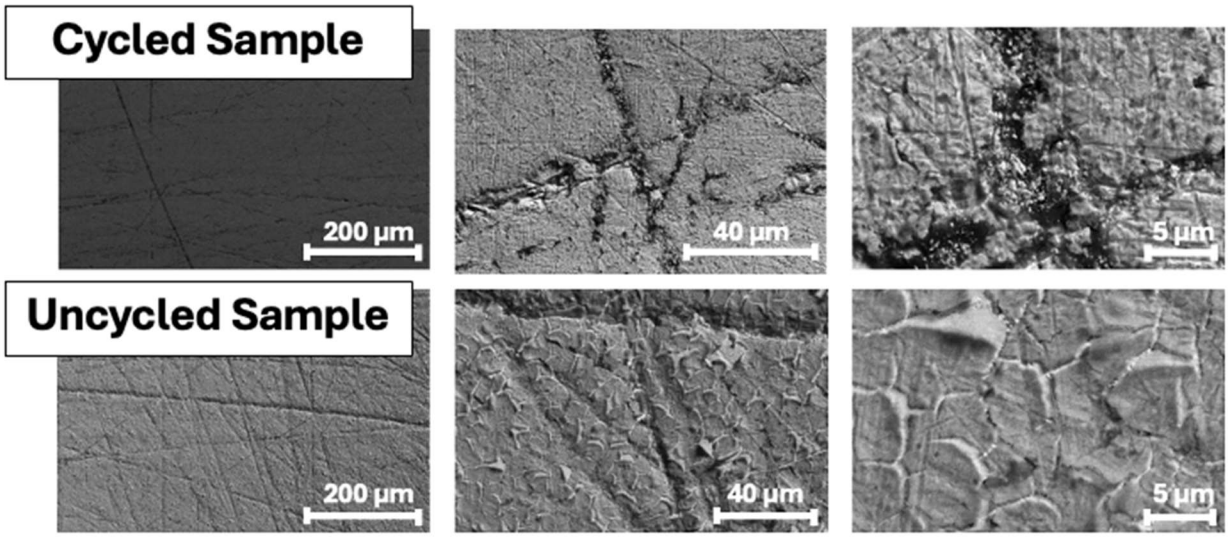

Figure 23: SEM Images of PB Film

SEM images of Prussian Blue thin films showing samples cycled in 1 M KNO_3 (top) and uncycled samples (bottom). From left to right, magnification increases from 200x to 1,200x to 5,000x.

In the uncycled sample, the PB film appears uniform across all magnifications and exhibits a flake-like morphology with visible grooves upon closer inspection. In contrast, the cycled sample no longer displays these flake structures, and the gold electrode surface is more exposed. The observed differences in image contrast are not attributed to a change in film color, but rather to variations in image acquisition settings. In some cases, darker SEM images may suggest a loss of conductivity in the sample. As seen in Figure 11, the optical microscope shows the film color and uniformity to be intact after cycling in KNO_3. However, the SEM results indicate a loss of conductivity and morphology changes, suggesting the film is delaminating at the microscopic level. Delamination is a phenomenon in which a film separates into layers, leading to the loss of electrochemically active material. The grooves observed in the uncycled sample may have served as sites for delamination during K^+ insertion and removal.

SEM imaging was coupled with EDX (Energy-Dispersive X-ray spectroscopy). EDX characterization is a technique that uses X-rays emitted by a sample to determine its elemental

composition and chemical state.[38] Both the cycled and uncycled films shown in Figure 23 were characterized using EDX to evaluate any changes in elemental ratios associated with electrochemical cycling.

Table 3: EDX Results

EDX results corresponding to the SEM images in Figure 22, comparing the atomic percentages of carbon, iron, gold, and potassium between cycled and uncycled Prussian Blue thin film samples.

Atom %	C	Fe	Au	K	Total %
Cycled	29.49 ± 0.17	4.19 ± 0.22	52.41 ± 0.20	1.11 ± 0.09	87.2 ± 0.1
Uncycled	28.34 ± 0.20	19.09 ± 0.34	47.95 ± 0.39	N/A	95.4 ± 0.1

The EDX results in Table 3 further support the claim that the PB film undergoes microscopic compositional changes after cycling in KNO_3. With cycling, the Fe content decreases significantly from 19% to 4%, while the Au percentage increases from 47% to 52%. These shifts suggest a thinning or partial delamination of the PB film which would lose Fe sites and expose more of the gold substrate. Interestingly, the carbon content is relatively consistent with cycling which is unexpected given the dramatic decrease in iron. This consistency implies that the carbon signal may not originate from the PB film alone, but could be attributed to other sources, such as residual carbon-based contamination or the substrate.

As expected, the K^+ content increases after cycling due to exposure to a cation-rich electrolyte. The low atomic percentage of potassium is expected as the electrochemical experiments end at +0.4 V vs SCE, a potential where the lattice should be free of K^+. The remaining potassium likely represents ions that are strongly bound or trapped within the film, offering valuable insight into the interaction between K^+ and the PB structure. Notably, the uncycled film shows no detected K^+ signal; a small residual signal was expected given the electrodeposition of the films involves KCl and other K^+ containing reagents. Its absence

indicates that K^+ is not initially incorporated into the lattice, suggesting that the ion insertion mechanism during cycling does not involve displacement of pre-existing cations.

2.2.5: Understanding the Effect of Electrolyte Cation on the Insertion Mechanism

Following the in-depth investigation of K^+ as the cycling cation interacting with PB thin films, we were interested to explore how other alkali metal cations with different atomic radii, i.e. Na^+ and Li^+, interact with the PB lattice. Both sodium and lithium share comparable electrical conductivity and low density with potassium, making them suitable candidates for comparative analysis. The initial assessment of how these cations insert into and are removed from the PB structure was carried out using cyclic voltammetry. Figure 24 presents the electrochemical behavior of K^+, Na^+, and Li^+ during repeated cycling within the PB thin film, providing insight into the similarities and differences in their interactions with the lattice over time.

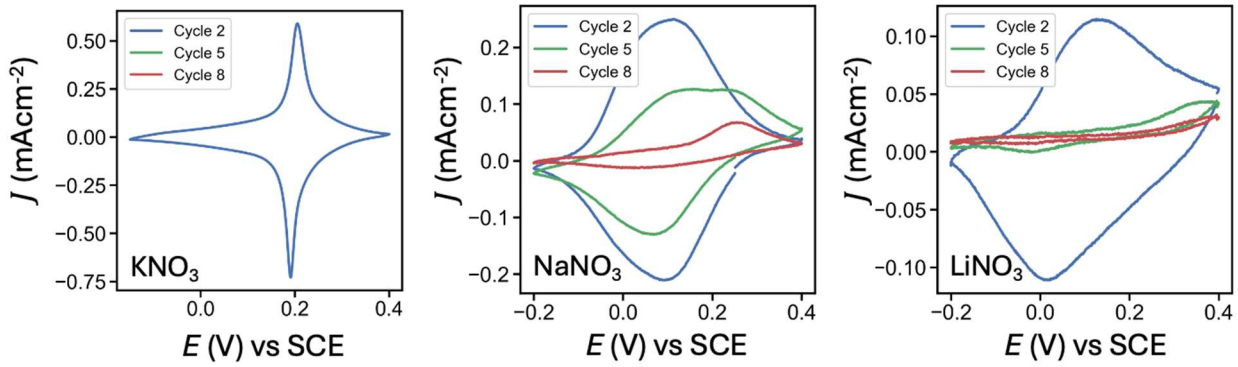

Figure 24: CVs of PB Thin Films with Various Cations

CV traces showing cation insertion and removal using various 1 M electrolytes across multiple cycles (cycles 2, 5, and 8). Data was collected at 20 mV/s using the electrochemical setup described in Figure 28.

As the cycling cation transitions from K^+ to Li^+, both the shape and magnitude of *J* change dramatically. In the case of KNO_3, the CV displays sharp and symmetric peaks that remain

consistent across cycles to the point of complete overlap, indicative of a highly reversible electrochemical reaction and a stable PB film. In contrast, when Na^+ is used as the inserting cation, the system response varies with cycle number. Although the first cycle shows symmetric peaks, they are significantly broader, and the magnitude is approximately half that observed for K^+. As cycling continues, the symmetry deteriorates; at cycle 5, the insertion and removal peaks start to split, forming two distinct humps. By cycle 8, the insertion peak vanishes entirely, and the removal peak shifts from +0.1 V to +0.2 V vs. SCE. These changes in peak shape and position suggest a different insertion/removal mechanism for Na^+ compared to K^+.[39]

This divergence becomes even more pronounced with Li^+. In $LiNO_3$, the magnitude of *J* is reduced by another factor of two compared to Na^+. By cycle 2, the CV no longer exhibits clear peak symmetry, and redox peaks do not have a distinct shape across the potential window. Unlike Na^+, where the current gradually declines between cycles 5 and 8, the Li^+ response decays rapidly. By cycle 5, the current density nears zero, and no redox peaks are visible. This behavior highlights a severe limitation in Li^+ insertion and suggests a fundamental difference in interaction with the PB lattice.

Comparing the long-term stability of PB films under cation cycling is essential, but to more effectively evaluate differences in peak shape and signal magnitude, it is useful to overlay the CV traces. Figure 25 presents an overlay of cycle 2 from Figure 23 for K^+, Na^+, and Li^+ to visually highlight the distinctions in electrochemical behavior.

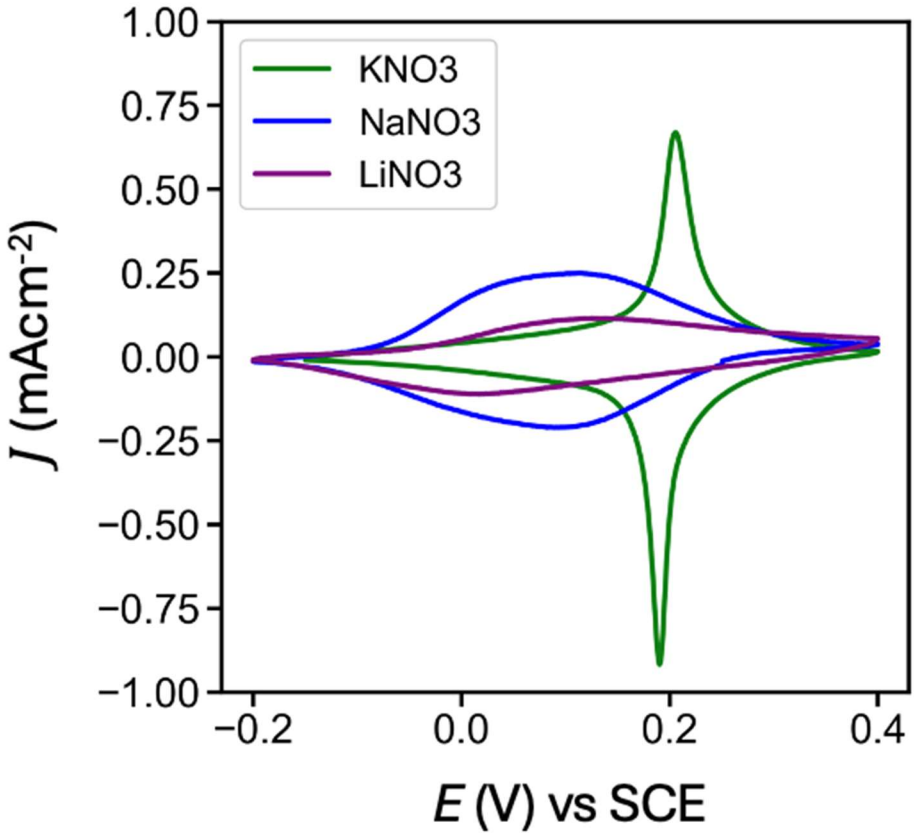

Figure 25: Direct Comparison of CV Character with Various Cations

Comparison of insertion and removal behavior for various cations during the second cycle of cyclic voltammograms (CVs) recorded in 1 M electrolytes. The measurements were performed at 20 mV/s using the electrochemical setup described in Figure 28.

This side-by-side comparison highlights distinct differences in both peak symmetry and current density, offering valuable insight into how each cation interacts with the PB lattice. As previously discussed, *J* decreases significantly in the order of decreasing cation size from K^+ to Na^+ to Li^+. Both K^+ and Na^+ exhibit relatively symmetric insertion and removal peaks, though the peak shapes and potentials differ noticeably. In contrast, the CV trace for Li^+ lacks sufficient signal intensity to clearly define peak positions or compare shapes, indicating poor electrochemical activity within the PB lattice. Regardless, the fact that all three cations generate

an initial response, even if it diminishes over time, indicates that some form of interaction with the PB film is occurring.

K^+, Na^+, and Li^+ were selected for this experiment due to their similar physical and electrochemical properties as members of the alkali metals family. A key difference across these cations, moving down the periodic table, is the increasing atomic radius: 1.23 Å for Li^+, 1.86 Å for Na^+, and 2.27 Å for K^+. The atomic radius plays an important role in chemical interactions, particularly in how each cation interacts with water molecules in aqueous electrolytes.

In solution, these cations become surrounded by a solvation shell, formed as the negative dipoles of water molecules orient around the positively charged ion for stabilization. When this shell is considered, the effective size of the ion is defined by its Stokes radius. Interestingly, the trend in Stokes radius is inversely related to atomic radius: Li^+ has the largest Stokes radius (4.8 Å), followed by Na^+ (4.6 Å), and then K^+ (3.6 Å).[40] This occurs because smaller, more charge-dense cations like Li^+ have higher hydration energies, meaning they hold onto their solvation shells more tightly. Hydration energy refers to the amount of energy required to strip the solvation shell from a cation. Since Li^+ has the strongest interaction with its hydration shell, it requires the most energy to shed it. In contrast, K^+, being larger and less charge-dense, has a weaker hydration shell and a lower hydration energy.

This solvation behavior is hypothesized to be a major factor influencing the electrochemical behavior of these cations in the PB lattice. Larger ions, like K^+, are more favorable to insert the PB lattice since they can more easily shed their hydration shells; even if partially solvated, the smaller Stokes radii lead to less structural disruption during cycling. Figure 26 presents a proposed mechanism illustrating how solvation shells affect PB lattice stability.

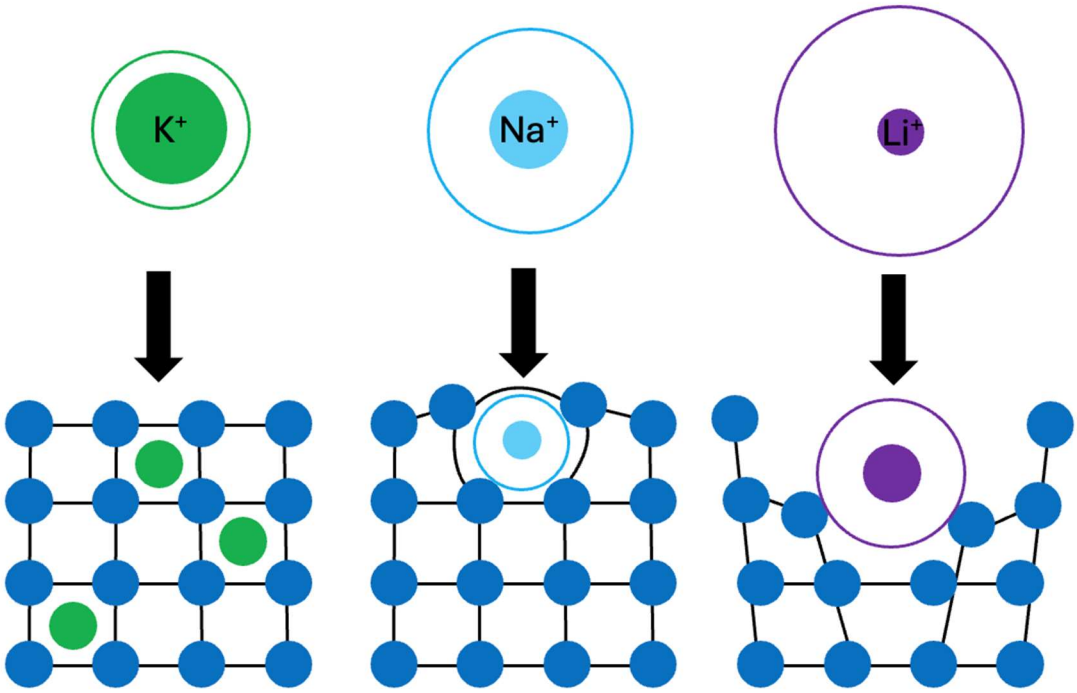

Figure 26: Proposed Insertion Mechanism for Different Cations

This schematic illustrates the structural effects on the PB thin film materials during Li, Na, and K insertion. The solid circles represent the atomic radius, and the rings represent the Stokes radius.

Before conducting the CV experiments, it was hypothesized that Li^+ and Na^+ ions would replace any K^+ ions originally present within the PB lattice as the films underwent cycling. However, EDX analysis (Table 3) revealed that no K^+ ions are initially present following electrodeposition, indicating that the cation exchange mechanism is not based on direct substitution.

Considering the Stokes radii, solvation shells, a proposed mechanism from Wi et al., the observed differences in the cyclic voltammogram responses can now be better understood.[41] The revised interpretation suggests that when Na^+ and Li^+ are cycled within the PB film, their strong solvation shells cannot be fully stripped. As these hydrated cations attempt to move through the

lattice, the larger effective sizes disrupt the structural integrity of the PB film, particularly in the upper layers, leading to film degradation.

If the Stokes radius exceeds the spatial constraints of the unit cell, it can cause structural breakdown of the PB lattice, specifically by disrupting bonds between the iron and cyano groups. In the case of Na^+, the slightly smaller Stokes radius compared to Li^+ results in a slower rate of degradation. The insertion and removal of Na^+ ions cause stretching of the lattice bonds, which must accommodate the larger ion. While the structure can initially adapt to balance the charge, continuous cycling eventually overstresses the bonds, leading to their rupture and overall film degradation. This interpretation is supported by visual observations at the working electrode. During Na^+ cycling, a noticeable lightening of the characteristic blue color of the PB film is seen on the Au substrate. In contrast, with Li^+, the effect is even more pronounced; by the end of the cycling experiments, the PB film is almost completely removed from the electrode surface. The larger Stokes radius of Li^+ causes even greater stretching of the lattice bonds, such that the film cannot withstand more than one or two insertion/removal cycles before the structure disintegrates.

2.4 Future Directions

Future work to better understand the interfacial ion transfer of cations into a Prussian Blue lattice should focus on completing the kinetic analysis and extracting rate constants to compare K^+ insertion and removal. Gaining insight into how the mechanism differs between cation insertion and removal will help refine the proposed model in Equation 11. Additionally, linear sweep voltammetry (LSV) could be employed to investigate the initial cycle of Na^+ and Li^+ insertion and removal into the lattice. Finally, Quartz Crystal Microbalance (QCM)

measurements should be conducted to determine the deposited mass of the Prussian Blue thin films.

Conclusion

In this thesis, I have aimed to describe why understanding the fundamentals of interfacial ion transfer is vital to the continued development of an environmentally friendly infrastructure. With electrochemistry being a key part in the development of clean energy technology, it is crucial to find the underlying mechanisms of degradation for systems like solar technology and energy storage.

Chapter 1 aimed to deconvolute the adsorption and nucleation characteristics involved in the reversible adsorption and stripping of $CuSO_4$ monolayers on an Au electrode surface. Building on the work of Hölzle, chronoamperometry was used to investigate the influence of temperature on nucleation and adsorption behavior.[12] Results showed that at lower temperatures, increased nucleation led to the formation of more ordered monolayers, as adsorbates had more time to diffuse across the surface to energetically favorable positions. In contrast, at elevated temperatures, random adsorption dominated, resulting in less ordered monolayers. Recognizing the significant role of temperature in determining surface morphology opens the door for future investigations into strategies for corrosion prevention. The research conducted with this model system serves as a foundation for understanding corrosion processes and their implications for modern technology.

Chapter 2 shifted focus to the mechanisms underlying much-needed energy storage devices. Using Prussian Blue as a model system, the phase transition to Prussian White and the resulting cation interactions with the lattice film provided a foundation for studying ion transfer processes. Previous work by Kuo and Thurman demonstrated that reversible adsorption mechanisms can be described using Equation 8, and similar electrochemical characteristics observed during the PB/PW phase transition suggested that this model could also apply to ion insertion and removal

mechanisms.[17,33] However, it was shown that the adsorption model alone does not fully capture the complexities of insertion and removal. Particularly when an aspect that remains poorly understood, diffusion of cations within the lattice, seems to become a significant factor. The research in this chapter sought to determine whether adsorption models can explain insertion behavior and to establish a basis for developing new models to further investigate degradation mechanisms in energy storage materials.

The work presented in this thesis aims to inform fundamental interfacial ion transfer mechanisms and improve electrochemical model systems, providing a foundation for the development of durable and sustainable electrochemical devices.

Experimental Methods

Copper System Experiments

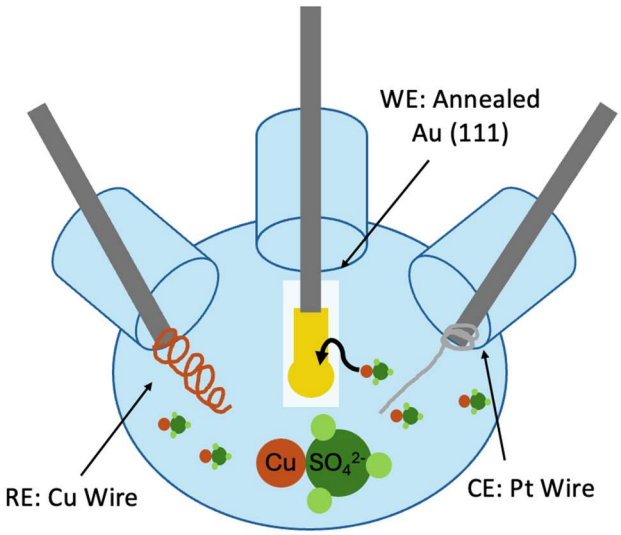

Figure 27: Electrochemical Cell for Copper Experiments.

Electrochemical cell setup for copper UPD, featuring an annealed pseudo-Au(111) working electrode, a platinum wire counter electrode, a copper wire reference electrode, and a $CuSO_4$ electrolyte.

Precleaned glass slides (Fisher Scientific) were solvent cleaned using a mixture of ethanol and water then O_2 plasma cleaned for 15 minutes. Using a mask to create desired form, 15 nm Ti followed by 200 nm of Au was electron-beam deposited using Angstrom Engineering's Vacuum Deposition System. Cut electrodes were annealed with a butane flame for 1 – 2 minutes, and a color change from brown to gold is seen at the edges. A cell containing 1mM copper oxide (CuO) in 10 mM sulfuric acid (96% H_2SO_4) electrolyte was purged with high purity Ar for 20 minutes. To control temperature conditions, a recirculating chiller with a 50:50 propylene glycol and water mixture was run through a jacketed cell. Using a Pt wire counter electrode and Cu wire reference electrode with Ar flowing along the surface, the Au(111) single crystal was cycled

using cyclic voltammetry (CV) at 25 mV/s until the current response was consistent between cycles.

After conditioning, one swipe of the butane flame was be used to reanneal the Au(111) surface. Placed in purged 10 mM H_2SO_4 with 1mM CuO electrolyte, CVs were run at 10 scan rates ranging from 1 mV/s to 1000 mV/s and voltage ranges were identified for the A and A' peaks across the potential window of 0 V vs Cu/Cu^{2+} and 0.9 V vs Cu/Cu^{2+}. Using chronoamperometry (CA), the voltage was held at a starting potential for 30 seconds before stepping at increments of 20 mV towards desired overpotential. The electrochemical data recorded with a SP-300 Potentiostat and analyzed using Python.

Prussian Blue System Experiments

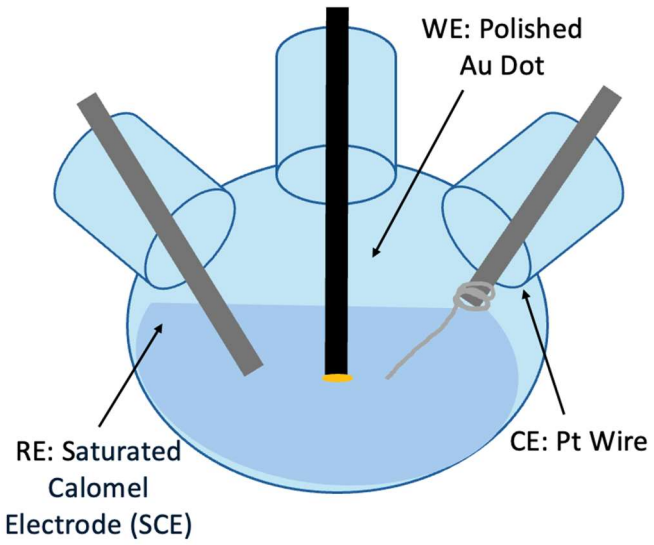

Figure 28: Electrochemical Cell for Prussian Blue Experiments

Electrochemical cell setup using a grit-polished Au dot working electrode, a platinum wire counter electrode, and a saturated calomel electrode (SCE) as the reference. The electrolyte composition varies depending on the cation and concentration used in the electrochemical experiments.

A BASi MF-2014 Au dot electrode was polished using abrasive paper with grit sizes of 30, 15, 9, 3, 2, and 1 microns for 30 seconds each. After sonicating for 5 minutes in 18.2 Ω deionized water (DI), the prepared electrode was placed in a three-necked cell containing a solution of 0.25 KCl with 0.5 mM $K_3Fe[CN]_6$ and 0.5 mM $Fe(NO_3)_3$. A platinum wire was used as a counter electrode and a saturated calomel electrode (SCE) for a reference. Electrodepositing a thin Prussian Blue (PB) film occurred as you apply a constant voltage of +0.3V vs SCE for 1 hour using the chronoamperometry (CA) technique.

After heavily quenching with 18.2 Ω deionized water, the PB film covered electrode was imaged on an OMAX Halogen Bulb optical microscope using ToupView software. The electrode was then placed in various electrolytes (varying with concentration from 10 mM to 1 M with LiNO3, NaNO3, and KNO3). The same platinum wire was placed in the cell after a quick swipe of a butane flame to remove any surface artifacts. A different saturated calomel electrode was used as the system reference for electrochemical testing. A SP-300 Biologic Potenitostat was used to run Potentio Electrochemical Impedance Spectroscopy (PEIS) and Cyclic Voltammetry (CV) techniques. PEIS measurements were taken from 1 MHz to 1 kHz with 6 points taken per decade. CVs were collected at 9 scan rates from 2 mV/s to 1000 mV/s between a potential range of -0.200 V vs SCE to 0.400 V vs SCE.

Bibliography

1. Xu, S.; Carter, E. A. Theoretical insights into heterogeneous (photo) electrochemical CO2 reduction. *Chemical reviews* **2018**, *119* (11), 6631-6669.
2. IEA (2022), World Energy Outlook 2022, IEA, Paris https://www.iea.org/reports/world-energy-outlook-2022, Licence: CC BY 4.0 (report); CC BY NC SA 4.0 (Annex A)
3. Santos, E.; Schmickler, W. Models of Electron Transfer at Different Electrode Materials. *Chemical Reviews* **2022**, *122* (12), 10581-10598. DOI: 10.1021/acs.chemrev.1c00583.
4. Kondo, Y.; Abe, T.; Yamada, Y. Kinetics of Interfacial Ion Transfer in Lithium-Ion Batteries: Mechanism Understanding and Improvement Strategies. *ACS Applied Materials & Interfaces* **2022**, *14* (20), 22706-22718. DOI: 10.1021/acsami.1c21683.
5. Gileadi, E. Problems in interfacial electrochemistry that have been swept under the carpet. *Journal of Solid State Electrochemistry* **2011**, *15*, 1359-1371.
6. *Renewables*. www.copper.org. https://www.copper.org/environment/sustainable-energy/renewables/.
7. Herrero, E.; Buller, L. J.; Abruña, H. D. Underpotential deposition at single crystal surfaces of Au, Pt, Ag and other materials. *Chemical Reviews* **2001**, *101* (7), 1897-1930.
8. Cai, C.; Ma, X.; Li, Y.; Zhou, R.; An, C.; Li, J. Investigation of copper underpotential deposition on polycrystalline gold electrodes. *International Journal of Electrochemical Science* **2023**, *18* (11), 100317.
9. Hou, P.; Chu, G.; Gao, J.; Zhang, Y.; Zhang, L. Li-ion batteries: Phase transition. *Chinese Physics B* **2015**, *25* (1), 016104.

10. Xu, C.; Yang, Z.; Zhang, X.; Xia, M.; Yan, H.; Li, J.; Yu, H.; Zhang, L.; Shu, J. Prussian blue analogues in aqueous batteries and desalination batteries. *Nano-micro letters* **2021**, *13*, 1-36.

11. Iannuzzi, M.; Frankel, G. The carbon footprint of steel corrosion. *npj Materials Degradation* **2022**, *6* (1), 101.

12. Hölzle, M.; Retter, U.; Kolb, D. The kinetics of structural changes in Cu adlayers on Au (111). *Journal of Electroanalytical Chemistry* **1994**, *371* (1-2), 101-109.

13. Hachiya, T.; Honbo, H.; Itaya, K. Detailed underpotential deposition of copper on gold (III) in aqueous solutions. *Journal of electroanalytical chemistry and interfacial electrochemistry* **1991**, *315* (1-2), 275-291.

14. Bosco, E.; Rangarajan, S. K. Some adsorption–nucleation-based models for electrochemical phase formation. *Journal of the Chemical Society, Faraday Transactions 1: Physical Chemistry in Condensed Phases* **1981**, *77* (7), 1673-1696.

15. Jerkiewicz, G.; Perreault, F.; Radovic-Hrapovic, Z. Effect of temperature variation on the under-potential deposition of copper on Pt (111) in aqueous H2SO4. *The Journal of Physical Chemistry C* **2009**, *113* (28), 12309-12316.

16. Gründer, Y.; Markovic, N. M.; Thompson, P.; Lucas, C. A. Temperature effects on the atomic structure and kinetics in single crystal electrochemistry. *Surface Science* **2015**, *631*, 123-129.

17. Thurman, K. A.; Cannan, C. M.; Shekhar, R.; Zhao, Y.; Boettcher, S. W.; Kempler, P. A. Anions in Corrosion: Influence of Polymer Electrolytes on the Interfacial Ion Transfer Kinetics of Cu at Au(111) Surfaces. *ACS Electrochemistry* **2025**, *1* (4), 425-432. DOI: 10.1021/acselectrochem.4c00181.

18. Ritchie, H.; Roser, M.; Rosado, P. *Energy Production and Consumption*. Our World in Data. https://ourworldindata.org/energy-production-consumption.

19. Lazard. 2024 *Levelized Cost of Energy+ Report*. https://www.lazard.com. https://www.lazard.com/research-insights/levelized-cost-of-energyplus/.

20. Korthauer, R. *Lithium-ion batteries: basics and applications*; Springer, 2018.

21. Streng, R. L.; Steeger, T.; Senyshyn, A.; Abel, S.; Schneider, P.; Benning, C.; Naranjo, B. M.; Gryc, D.; Hussain, M. Z.; Lieleg, O. A low-cost and high-energy aqueous potassium-ion battery. *Journal of Energy Chemistry* **2025**, *106*, 523-531.

22. Shepard, P. *Potassium-Ion Rechargeable Batteries for a Sustainable Environment*. Eepower.com. https://eepower.com/news/potassium-ion-rechargeable-batteries-for-a-sustainable-environment/ (accessed 2025-04-27).

23. Bárcena Soto, M.; Scholz, F. The thermodynamics of the insertion electrochemistry of solid metal hexacyanometallates. *Journal of Electroanalytical Chemistry* **2002**, *521* (1), 183-189. DOI: https://doi.org/10.1016/S0022-0728(02)00710-6.

24. Huggins, R. Review—A New Class of High Rate, Long Cycle Life, Aqueous Electrolyte Battery Electrodes. *Journal of The Electrochemical Society* **2017**, *164*, A5031-A5036. DOI: 10.1149/2.0571701jes.

25. García-Jareño, J.; Sanmatías, A.; Navarro-Laboulais, J.; Vicente, F. The role of potassium and hydrogen ions in the Prussian Blue⇄ Everitt's Salt process. *Electrochimica acta* **1998**, *44* (2-3), 395-405.

26. Fu, Z.; Wei, Y.; Liu, W.; Li, J.; Li, J.; Ma, Y.; Zhang, X.; Yan, Y. Investigation of electrochromic device based on multi-step electrodeposited PB films. *Ionics* **2021**, *27*, 4419-4427.

27. Bayzi Isfahani, V.; Arab, A.; Horta Belo, J.; Pedro Araújo, J.; Manuela Silva, M.; Gonçalves Almeida, B. Comparison of physical/chemical properties of Prussian blue thin films prepared by different pulse and DC electrodeposition methods. *Materials* **2022**, *15* (24), 8857.

28. Pathak, P. K.; Agrim, K. P.; Park, C.; Ahn, H.; Salunkhe, R. R. Elevating the Performance of the Prussian Blue Analogue Cathode for Sodium-Ion Batteries by Adjusting the Low Spin Fe Redox. *ACS Applied Energy Materials* **2024**. DOI: 10.1021/acsaem.3c03262.

29. Lundgren, C.; Murray, R. W. Observations on the composition of Prussian blue films and their electrochemistry. *Inorganic Chemistry* **1988**, *27* (5), 933-939.

30. Kraft, A. Some considerations on the structure, composition, and properties of Prussian blue: a contribution to the current discussion. *Ionics* **2021**, *27* (6), 2289-2305. DOI: 10.1007/s11581-021-04013-0.

31. Nakanishi, S.; Lu, G.; Kothari, H. M.; Bohannan, E. W.; Switzer, J. A. Epitaxial electrodeposition of prussian blue thin films on single-crystal Au (110). *Journal of the American Chemical Society* **2003**, *125* (49), 14998-14999.

32. Isfahani, V. B.; Memarian, N.; Dizaji, H. R.; Arab, A.; Silva, M. M. The physical and electrochromic properties of Prussian Blue thin films electrodeposited on ITO electrodes. *Electrochimica Acta* **2019**, *304*, 282-291.

33. Kuo, D.-Y.; Lu, X.; Hu, B.; Abruña, H. D.; Suntivich, J. Rate and mechanism of electrochemical formation of surface-bound hydrogen on Pt (111) single crystals. *The Journal of Physical Chemistry Letters* **2022**, *13* (27), 6383-6390.

34. Lazanas, A. C.; Prodromidis, M. I. Electrochemical impedance spectroscopy─ a tutorial. *ACS measurement science au* **2023**, *3* (3), 162-193.

35. Bard, A. J.; Faulkner, L. R.; White, H. S. *Electrochemical methods: fundamentals and applications*; John Wiley & Sons, 2022.

36. Christmann, K.; Ertl, G.; Pignet, T. Adsorption of hydrogen on a Pt (111) surface. *Surface Science* **1976**, *54* (2), 365-392.

37. Hao, X.; Yan, T.; Wang, Z.; Liu, S.; Liang, Z.; Shen, Y.; Pritzker, M. Unipolar pulse electrodeposition of nickel hexacyanoferrate thin films with controllable structure on platinum substrates. *Thin Solid Films* **2012**, *520* (7), 2438-2448.

38. Isfahani, V. B.; Memarian, N.; Dizaji, H. R.; Arab, A.; Silva, M. M. The physical and electrochromic properties of Prussian Blue thin films electrodeposited on ITO electrodes. *Electrochimica Acta* **2019**, *304*, 282-291.

39. Erinmwingbovo, C.; Palagonia, M. S.; Brogioli, D.; La Mantia, F. Intercalation into a Prussian blue derivative from solutions containing two species of cations. *ChemPhysChem* **2017**, *18* (8), 917-925.

40. Mahler, J.; Persson, I. A study of the hydration of the alkali metal ions in aqueous solution. *Inorganic chemistry* **2012**, *51* (1), 425-438.

41. Wi, T.-U.; Park, C.; Ko, S.; Kim, T.; Choi, A.; Muralidharan, V.; Choi, M.; Lee, H.-W. Cathode electrolyte interphase engineering for Prussian blue analogues in lithium-ion batteries. *Nano Letters* **2024**, *24* (25), 7783-7791.

42. Christmann, K.; Ertl, G.; Pignet, T. Adsorption of hydrogen on a Pt (111) surface. *Surface Science* **1976**, *54* (2), 365-392.